



HAL
open science

Robin-Robin loose coupling for incompressible fluid-structure interaction: non-linear setting and nearly-optimal error analysis

Erik Burman, Rebecca Durst, Miguel Angel Fernández, Johnny Guzmán,
Oscar Ruz

► To cite this version:

Erik Burman, Rebecca Durst, Miguel Angel Fernández, Johnny Guzmán, Oscar Ruz. Robin-Robin loose coupling for incompressible fluid-structure interaction: non-linear setting and nearly-optimal error analysis. 2023. hal-04258861v1

HAL Id: hal-04258861

<https://inria.hal.science/hal-04258861v1>

Preprint submitted on 25 Oct 2023 (v1), last revised 27 Oct 2023 (v2)

HAL is a multi-disciplinary open access archive for the deposit and dissemination of scientific research documents, whether they are published or not. The documents may come from teaching and research institutions in France or abroad, or from public or private research centers.

L'archive ouverte pluridisciplinaire **HAL**, est destinée au dépôt et à la diffusion de documents scientifiques de niveau recherche, publiés ou non, émanant des établissements d'enseignement et de recherche français ou étrangers, des laboratoires publics ou privés.



Distributed under a Creative Commons Attribution 4.0 International License

40 scheme without loss of stability (see also [2]). Robin conditions had been shown to
 41 perform well as a preconditioner already in [1]. In [9], the Robin coefficient inher-
 42 ited the $\mathcal{O}(h^{-1})$ scaling from Nitsche’s method, but it was noted numerically that
 43 this scaling appeared not to be necessary for the stability of the algorithm. In a re-
 44 cent development [7], it was shown for a semi-discretization in time that the coupling
 45 scheme indeed is stable independent of the added mass effect and an error estimate of
 46 order $\mathcal{O}(\tau^{\frac{1}{2}})$, where τ denotes the time step, was shown. Another result in this spirit
 47 was reported in [24], for a fully discrete Robin-Robin method and under a CFL-like
 48 condition on the discretization parameters. A stability estimate for the time semi-
 49 discretized problem with moving fluid domain is also provided, but the treatment
 50 of the convective term involves an artificial modification of the fluid velocity on the
 51 interface. An alternative fully discrete formulation is introduced in [5], where the
 52 stresses are represented in terms of Lagrange multipliers or variational residuals, and
 53 the exponential growth of the stability factor was moderated to sub-linear growth
 54 without conditions on the discretization parameters. Finally, both for the cases of
 55 parabolic-parabolic and parabolic-hyperbolic couplings, it was shown in [6] that in
 56 most situations one can expect the nearly-optimal order $\mathcal{O}(\tau\sqrt{1 + \log \tau^{-1}})$. Depend-
 57 ing on the physical parameters however it was noted that this may not be attained,
 58 except for very small time steps unless the parameter in the Robin condition is chosen
 59 carefully.

60 The objective of the present paper is to build on the results of [5, 6] and extend
 61 them to more realistic settings, showing that the Robin-Robin loose coupling is indeed
 62 expected to result in a first order time discretization scheme also in physically relevant
 63 situations. The scientific contributions of this work are three fold. First, in a fully
 64 non-linear setting (coupling viscous incompressible flow in moving domains with the
 65 dynamics of an hyper-elastic solid), we provide a rigorous fully discrete formulation
 66 with suitable stabilization terms which guarantee unconditional energy stability. Sec-
 67 ond, in the linear case, we present the extension of the nearly-optimal error analysis
 68 from [6] to the case of the Stokes-elasticity system. To the best of our knowledge,
 69 this is the first time that such accuracy is proved for a loosely coupled scheme in
 70 incompressible fluid-structure interaction involving thick-walled solids. The latter re-
 71 sults were first reported in [12, Chapter 5] and, therefore, the proofs are only sketched
 72 herein. Finally, the accuracy properties of the proposed method are illustrated in a
 73 series of well-known numerical examples. We in particular investigate the dependence
 74 of the accuracy on the physical parameters and the choice of parameter in the Robin
 75 coupling.

76 The rest of the paper is organized as follows. In Section 2, we introduce the
 77 considered physically realistic setting. We show how to extend the fully discrete
 78 formulation of [5] to this nonlinear case and prove the fundamental stability estimate
 79 in Section 3. Section 4 is devoted to the derivation of the nearly-optimal error estimate
 80 in a simplified linear setting. Finally, the paper is ended with some numerical examples
 81 which are reported in Section 5.

82 **2. Problem setting.** We consider a fluid-structure interaction system in which
 83 the fluid is modeled by the incompressible Navier-Stokes equations, in arbitrary
 84 Lagrangian-Eulerian (ALE) formalism, and the solid by the non-linear elastody-
 85 namics equations. The reference configuration of system is given by the domain
 86 $\Omega \stackrel{\text{def}}{=} \Omega^f \cup \Omega^s \subset \mathbb{R}^d$, with $d = 2, 3$. For all time $t > 0$, the current solid configuration
 87 is denoted by $\Omega^s(t) \subset \mathbb{R}^d$, whereas $\Omega^f(t) \subset \mathbb{R}^d$ stands for the moving fluid control
 88 volume. We denote by $\Sigma(t) \stackrel{\text{def}}{=} \partial\Omega^f(t) \cap \partial\Omega^s(t)$ the current configuration of the fluid-

89 structure interface, whose reference configurations corresponds to $\Sigma \stackrel{\text{def}}{=} \partial\Omega^f \cap \partial\Omega^s$.
 90 The remaining parts of the fluid and solid boundaries are supposed to be time inde-
 91 pendent and partitioned as $\partial\Omega^f = \Gamma^f \cup \Sigma$ and $\partial\Omega^s = \Gamma^s \cup \Sigma$.

The moving fluid domain $\Omega^f(t)$ can be parametrized in terms of the so-called ALE map, $\mathcal{A} : \Omega^f \times \mathbb{R}^+ \rightarrow \mathbb{R}^d$, in such a way that $\Omega^f(t) = \mathcal{A}(\Omega^f, t)$. The ALE deformation map \mathcal{A} is often written in terms of fluid domain displacement $\mathbf{d}^f : \Omega^f \times \mathbb{R}^+ \rightarrow \mathbb{R}^d$ via the relation $\mathcal{A} = \mathbf{I}_{\Omega^f} + \mathbf{d}^f$, where \mathbf{I}_{Ω^f} stands for the identity operator in Ω^f . We can hence introduce the notation $\mathcal{A}_t \stackrel{\text{def}}{=} \mathcal{A}(\cdot, t)$, the fluid domain velocity $\mathbf{w} \stackrel{\text{def}}{=} \partial_t \mathcal{A} = \partial_t \mathbf{d}^f$, the fluid gradient of deformation $\mathbf{F} \stackrel{\text{def}}{=} \nabla \mathcal{A}$ (spatial gradient) and its Jacobian $J \stackrel{\text{def}}{=} \det \mathbf{F}$. For a given field f defined in the current configuration $\Omega^f(t)$, we shall use the notation \hat{f} to defined its corresponding ALE description in Ω^f , by composing with the ALE map, namely,

$$\hat{f}(\mathbf{x}, t) \stackrel{\text{def}}{=} f(\mathcal{A}(\mathbf{x}, t), t) \quad \forall \mathbf{x} \in \Omega^f.$$

92 Conversely, a given field defined in the reference configuration Ω^f can also be trans-
 93 ported into the current configuration by composition with \mathcal{A}_t^{-1} . For the sake of
 94 simplicity, this composition is omitted. For instance, \mathbf{w} in (2.1)₁ below has to be read
 95 as $\mathbf{w} \circ \mathcal{A}_t^{-1}$.

96 **Coupled problem in strong form.** The considered fluid-structure interaction
 97 model reads as follows: find the fluid domain displacement $\mathbf{d}^f : \Omega^f \times \mathbb{R}^+ \rightarrow \mathbb{R}^d$, the
 98 fluid velocity $\hat{\mathbf{u}} : \Omega^f \times \mathbb{R}^+ \rightarrow \mathbb{R}^d$, the fluid pressure $\hat{p} : \Omega^f \times \mathbb{R}^+ \rightarrow \mathbb{R}$, the solid
 99 displacement $\mathbf{d} : \Omega^s \times \mathbb{R}^+ \rightarrow \mathbb{R}^d$, and the structure velocity $\dot{\mathbf{d}} : \Omega^s \times \mathbb{R}^+ \rightarrow \mathbb{R}^d$ such
 100 that, for all $t > 0$,

$$101 \quad (2.1) \quad \begin{cases} \rho^f \partial_t \mathbf{u}|_{\mathcal{A}} + \rho^f (\mathbf{u} - \mathbf{w}) \cdot \nabla \mathbf{u} - \operatorname{div} \boldsymbol{\sigma}(\mathbf{u}, p) = \mathbf{0} & \text{in } \Omega^f(t), \\ \operatorname{div} \mathbf{u} = 0 & \text{in } \Omega^f(t), \\ \mathbf{u} = \mathbf{0} & \text{on } \Gamma^f, \end{cases}$$

$$102 \quad (2.2) \quad \begin{cases} \rho^s \partial_t \dot{\mathbf{d}} - \operatorname{div} (\mathbf{F}^s \boldsymbol{\Sigma}(\mathbf{d})) = \mathbf{0} & \text{in } \Omega^s, \\ \dot{\mathbf{d}} = \partial_t \mathbf{d} & \text{in } \Omega^s, \\ \mathbf{d} = \mathbf{0} & \text{on } \Gamma^s, \end{cases}$$

$$103 \quad (2.3) \quad \begin{cases} \mathbf{d}^f = \mathcal{L}(\mathbf{d}|_{\Sigma}), \quad \mathbf{w} = \partial_t \mathbf{d}^f, \quad \mathcal{A} = \mathbf{I}_{\Omega^f} + \mathbf{d}^f, \quad \Omega^f(t) = \mathcal{A}(\Omega^f, t), \\ \hat{\mathbf{u}} = \dot{\mathbf{d}} & \text{on } \Sigma, \\ \mathbf{F}^s \boldsymbol{\Sigma}(\mathbf{d}) \mathbf{n}^s = -J \hat{\boldsymbol{\sigma}}(\mathbf{u}, p) \mathbf{F}^{-T} \hat{\mathbf{n}} & \text{on } \Sigma. \end{cases}$$

The constants $\rho^f, \rho^s > 0$ stand, respectively, for the fluid and solid densities, $\partial_t|_{\mathcal{A}} \stackrel{\text{def}}{=} \partial_t + \mathbf{w} \cdot \nabla$ for the ALE time derivative and $\boldsymbol{\sigma}(\mathbf{u}, p) \stackrel{\text{def}}{=} 2\mu \boldsymbol{\epsilon}(\mathbf{u}) - p \mathbf{I}$ for the fluid Cauchy stress tensor, with $\mu > 0$ the fluid dynamic viscosity (supposed constant) and $\boldsymbol{\epsilon}(\mathbf{u}) = \frac{1}{2}(\nabla \mathbf{u} + (\nabla \mathbf{u})^T)$ the strain rate tensor. The symbol $\mathbf{F}^s \stackrel{\text{def}}{=} \mathbf{I} + \nabla \mathbf{d}$ corresponds to the gradient of deformation of the solid and $\boldsymbol{\Sigma}(\mathbf{d})$ denotes its second Piola-Kirchhoff stress tensor which, for an hyper-elastic material, is given in terms of the internal energy functional $W : \mathbb{R}_{\text{sym}}^{d \times d} \rightarrow \mathbb{R}^+$ as

$$\boldsymbol{\Sigma} = \frac{\partial W}{\partial \mathbf{E}}(\mathbf{E}),$$

104 where the symbol \mathbf{E} denotes the Green-Lagrange strain tensor given by the relation
 105 $\mathbf{E} \stackrel{\text{def}}{=} \frac{1}{2}((\mathbf{F}^s)^\top \mathbf{F}^s - \mathbf{I})$.

106 Finally, the coupled system (2.1)-(2.3) is complemented with the following initial
 107 conditions $\hat{\mathbf{u}}(0) = \hat{\mathbf{u}}_0$ and $\mathbf{d}(0) = \mathbf{d}_0, \dot{\mathbf{d}}(0) = \dot{\mathbf{d}}_0$ in Ω^f and Ω^s , respectively.

108 The relation (2.3)₁ enforces the geometrical compatibility between the fluid and
 109 solid domains. Here, the symbol \mathcal{L} represents a smooth lifting operator (possibly
 110 non-linear) from Σ over Ω^f , which vanishes on Γ^f . The remaining interface conditions
 111 (2.3)_{2,3} enforce, respectively, the so-called interface kinematic and dynamic coupling.

Weak form and energy identity. We consider the following functional spaces:

$$\mathbf{V}^f \subset \{\mathbf{v} \in \mathbf{H}^1(\Omega^f) : \mathbf{v}|_{\Gamma^f} = \mathbf{0}\}, \quad M^f \stackrel{\text{def}}{=} L^2(\Omega^f), \quad \mathbf{V}^s \subset \{\mathbf{v} \in \mathbf{H}^1(\Omega^s) : \mathbf{v}|_{\Gamma^s} = \mathbf{0}\}.$$

112 Let $(\hat{\mathbf{u}}, \hat{p}, \hat{\mathbf{d}}, \boldsymbol{\xi})$ be solution of the coupled system (2.1)-(2.3), one can show that the
 113 following monolithic variational formulation holds (see, e.g., [15]), for $t > 0$,

$$(2.4) \quad \begin{aligned} 114 \quad & \rho^f \frac{d}{dt} \int_{\Omega^f(t)} \mathbf{u} \cdot \mathbf{v} - \rho^f \int_{\Omega^f(t)} (\operatorname{div} \mathbf{w}) \mathbf{u} \cdot \mathbf{v} + \rho^f \int_{\Omega^f(t)} (\mathbf{u} - \mathbf{w}) \cdot \nabla \mathbf{u} \cdot \mathbf{v} + 2\mu \int_{\Omega^f(t)} \boldsymbol{\epsilon}(\mathbf{u}) : \boldsymbol{\epsilon}(\mathbf{v}) \\ 115 \quad & - \int_{\Omega^f(t)} p \operatorname{div} \mathbf{v} + \int_{\Omega^f(t)} q \operatorname{div} \mathbf{u} + \rho^s \int_{\Omega^s} \partial_t \dot{\mathbf{d}} \cdot \boldsymbol{\xi} + \int_{\Omega^s} \boldsymbol{\Sigma} : \partial_{\mathbf{d}}(\mathbf{E}) \boldsymbol{\xi} = 0 \end{aligned}$$

116 for all $(\hat{\mathbf{v}}, \hat{q}, \boldsymbol{\xi}) \in \mathbf{V}^f \times M^f \times \mathbf{V}^s$ with $\hat{\mathbf{v}}|_{\Sigma} = \boldsymbol{\xi}|_{\Sigma}$, and where we have used the notation

$$117 \quad (2.5) \quad \partial_{\mathbf{d}}(\mathbf{E}) \boldsymbol{\xi} \stackrel{\text{def}}{=} \frac{1}{2} \left[(\mathbf{F}^s)^\top \nabla \boldsymbol{\xi} + (\nabla \boldsymbol{\xi})^\top \mathbf{F}^s \right],$$

118 for the differential of \mathbf{E} applied to $\boldsymbol{\xi}$.

119 By testing (2.4) with $(\hat{\mathbf{v}}, \hat{q}, \boldsymbol{\xi}) = (\hat{\mathbf{u}}, \hat{p}, \hat{\mathbf{d}})$ and using standard arguments, we can
 120 obtain the following classical energy identity (see, e.g., [15]):

$$(2.6) \quad \begin{aligned} 121 \quad & \frac{\rho^f}{2} \|\mathbf{u}\|_{0, \Omega^f(t)}^2 + \frac{\rho^s}{2} \|\dot{\mathbf{d}}\|_{0, \Omega^s}^2 + \int_{\Omega^s} W(\mathbf{E}(\mathbf{d})) + 2\mu \int_0^t \|\boldsymbol{\epsilon}(\mathbf{u}(s))\|_{0, \Omega^f(s)}^2 ds \\ 122 \quad & = \frac{\rho^f}{2} \|\mathbf{u}_0\|_{0, \Omega^f(0)}^2 + \frac{\rho^s}{2} \|\dot{\mathbf{d}}_0\|_{0, \Omega^s}^2 + \frac{1}{2} \int_{\Omega^s} W(\mathbf{E}(\mathbf{d}_0)). \end{aligned}$$

123 Here, the first two terms represent the kinetic energy of the fluid and solid, respec-
 124 tively. The third term takes into account the hyperelastic energy of the solid, and the
 125 fourth term corresponds to the viscous dissipation of the fluid.

126 **3. Robin-Robin explicit coupling scheme.** The purpose of this section is to
 127 formulate the Robin-Robin loosely coupled scheme of [5, 7] in the framework of the
 128 non-linear coupled problem (2.1)-(2.3).

Time semi-discretization. In what follows, the scalar $\tau > 0$ denotes the time-
 step length and $\{t_n \stackrel{\text{def}}{=} n\tau\}_{n \in \mathbb{N}}$ represents the temporal grid. We shall also make use
 of the following notations:

$$\partial_\tau x^n \stackrel{\text{def}}{=} \frac{1}{\tau} (x^n - x^{n-1}), \quad x^{n-\frac{1}{2}} \stackrel{\text{def}}{=} \frac{1}{2} (x^n + x^{n-1}),$$

129 for the first-order backward difference and the mid-point value, respectively. More-
 130 over, for a given time-dependent quantity $x(t)$, we will use the notation $x^n \stackrel{\text{def}}{=} x(t_n)$.

131 The bulk terms of the fluid sub-system (2.1) will be discretized in time with
 132 a backward-Euler semi-implicit scheme, whereas for the solid sub-system (2.2) we
 133 consider a mid-point scheme with the so-called Gonzalez correction (see [20]). Finally,
 134 for the time discretization of the interface conditions (2.3), we combine an explicit
 135 treatment of the geometrical compatibility with a Robin-Robin type splitting of the
 136 kinematic and dynamic interface conditions, originally proposed in [7] for the linear
 137 case. By introducing the following notation for the interfacial fluid stresses on the
 138 reference configuration,

$$139 \quad (3.1) \quad \boldsymbol{\lambda}^n \stackrel{\text{def}}{=} J^n \hat{\boldsymbol{\sigma}}(\mathbf{u}^n, p^n) (\mathbf{F}^n)^{-T} \hat{\mathbf{n}} \quad \text{on } \Sigma,$$

140 the resulting time-stepping procedure can formally be written as follows:

141 • Solve solid:

$$142 \quad (3.2) \quad \left\{ \begin{array}{l} \rho^s \partial_\tau \dot{\mathbf{d}}^n - \text{div} \left(\mathbf{F}^{\text{s},n-\frac{1}{2}} \bar{\boldsymbol{\Sigma}}^{n-\frac{1}{2}} \right) = \mathbf{0} \quad \text{in } \Omega^s, \\ \dot{\mathbf{d}}^{n-\frac{1}{2}} = \partial_\tau \mathbf{d}^n \quad \text{in } \Omega^s, \\ \mathbf{d}^n = \mathbf{0} \quad \text{on } \Gamma^s, \\ \mathbf{F}^{\text{s},n-\frac{1}{2}} \bar{\boldsymbol{\Sigma}}^{n-\frac{1}{2}} \mathbf{n}^s + \alpha (\dot{\mathbf{d}}^{n-\frac{1}{2}} - \hat{\mathbf{u}}^{n-1}) = -\boldsymbol{\lambda}^{n-1} \quad \text{on } \Sigma. \end{array} \right.$$

143 • Fluid domain update:

$$144 \quad (3.3) \quad \mathbf{d}^{\text{f},n} = \mathcal{L}(\mathbf{d}^n|_\Sigma), \quad \mathbf{w}^n = \partial_\tau \mathbf{d}^{\text{f},n}, \quad \mathcal{A}^n = \mathbf{I}_{\Omega^f} + \mathbf{d}^{\text{f},n}, \quad \Omega^{\text{f},n} = \mathcal{A}^n(\Omega^f).$$

145 • Solve fluid:

$$146 \quad (3.4) \quad \left\{ \begin{array}{l} \rho^f \partial_\tau \mathbf{u}^n|_{\mathcal{A}} + \rho^f (\mathbf{u}^{n-1} - \mathbf{w}^n) \cdot \nabla \mathbf{u}^n - \text{div} \boldsymbol{\sigma}(\mathbf{u}^n, p^n) = \mathbf{0} \quad \text{in } \Omega^{\text{f},n}, \\ \text{div} \mathbf{u}^n = 0 \quad \text{in } \Omega^{\text{f},n}, \\ \mathbf{u}^n = \mathbf{0} \quad \text{on } \Gamma^f, \\ \boldsymbol{\lambda}^n + \alpha (\hat{\mathbf{u}}^n - \dot{\mathbf{d}}^{n-\frac{1}{2}}) = \boldsymbol{\lambda}^{n-1} \quad \text{on } \Sigma. \end{array} \right.$$

147 Here, the symbol $\bar{\boldsymbol{\Sigma}}^{n-\frac{1}{2}}$ denotes the mid-point correction of the solid stress given by
 148 (see [20]):

$$149 \quad (3.5) \quad \bar{\boldsymbol{\Sigma}}^{n-\frac{1}{2}} \stackrel{\text{def}}{=} \boldsymbol{\Sigma}^{n-\frac{1}{2}} + \frac{\partial_\tau W(\mathbf{E}^n) - \frac{\partial W}{\partial \mathbf{E}}(\mathbf{E}^{n-\frac{1}{2}}) : \partial_\tau \mathbf{E}^n}{|\partial_\tau \mathbf{E}^n|^2} \partial_\tau \mathbf{E}^n,$$

150 which guarantees energy stability in the solid, and the scalar $\alpha > 0$ stands for the user-
 151 defined Robin parameter of the fluid-solid splitting. Note that the above interfacial
 152 Robin-Robin splitting, viz.,

$$153 \quad (3.6) \quad \left\{ \begin{array}{l} \mathbf{F}^{\text{s},n-\frac{1}{2}} \bar{\boldsymbol{\Sigma}}^{n-\frac{1}{2}} \mathbf{n}^s + \alpha (\dot{\mathbf{d}}^{n-\frac{1}{2}} - \hat{\mathbf{u}}^{n-1}) = -\boldsymbol{\lambda}^{n-1} \quad \text{on } \Sigma, \\ \boldsymbol{\lambda}^n + \alpha (\hat{\mathbf{u}}^n - \dot{\mathbf{d}}^{n-\frac{1}{2}}) = \boldsymbol{\lambda}^{n-1} \quad \text{on } \Sigma, \end{array} \right.$$

154 is written in the reference configuration of the interface.

155 **Space discretization, fully discrete scheme.** For the spatial discretization of
 156 (3.2)–(3.4), we adopt a finite element approximation. Let \mathcal{T}_h^f and \mathcal{T}_h^s be, respectively,
 157 simplicial triangulations of Ω^f and Ω^s . We assume that \mathcal{T}_h^f and \mathcal{T}_h^s match on the
 158 interface Σ . We then define the following finite element spaces:

$$159 \quad \mathbf{V}_h^s \stackrel{\text{def}}{=} \{ \mathbf{v} \in \mathbf{V}^s : \mathbf{v}|_K \in \mathbb{P}^1(K), \forall K \in \mathcal{T}_h^s \}, \quad \mathbf{V}_h^f \stackrel{\text{def}}{=} \{ \mathbf{v} \in \mathbf{V}^f : \mathbf{v}|_K \in \mathbb{P}^1(K), \forall K \in \mathcal{T}_h^f \},$$

$$160 \quad M_h^f \stackrel{\text{def}}{=} \{ v \in M^f : v|_K \in \mathbb{P}^1(K), \forall K \in \mathcal{T}_h^f \},$$

161 Since the fluid and solid meshes are assumed to match at the interface, we can define
 162 the discrete traces space

$$163 \quad (3.7) \quad \mathbf{V}_h^g \stackrel{\text{def}}{=} \text{Tr}_\Sigma \mathbf{V}_h^f = \text{Tr}_\Sigma \mathbf{V}_h^s.$$

164 The fluid bi-linear form is given by

$$(3.8) \quad a_{\Omega^{f,n}}(\mathbf{u}_h^{n-1}, \mathbf{w}_h^n; (\mathbf{u}_h^n, p_h^n), (\mathbf{v}_h, q_h)) \stackrel{\text{def}}{=} \rho^f \int_{\Omega^{f,n}} (\mathbf{u}_h^{n-1} - \mathbf{w}_h^n) \cdot \nabla \mathbf{u}_h^n \cdot \mathbf{v}_h$$

$$+ \frac{\rho^f}{2} \int_{\Omega^{f,n}} (\text{div } \mathbf{u}_h^{n-1}) \mathbf{u}_h^n \cdot \mathbf{v}_h$$

$$165 \quad - \frac{\rho^f}{2} \int_{\Sigma^n} (\mathbf{u}_h^{n-1} - \hat{\mathbf{d}}_h^{n-\frac{1}{2}}) \cdot \mathbf{n} \mathbf{u}_h^n \cdot \mathbf{v}_h$$

$$+ 2\mu \int_{\Omega^{f,n}} \boldsymbol{\epsilon}_h(\mathbf{u}_h^n) : \boldsymbol{\epsilon}_h(\mathbf{v}_h) - \int_{\Omega^{f,n}} p_h^n \text{div } \mathbf{v}_h$$

$$+ \int_{\Omega^{f,n}} q_h \text{div } \mathbf{u}_h^n$$

$$+ s_h^f(\mathbf{u}_h^{n-1}, \mathbf{w}_h^n; (\mathbf{u}_h^n, p_h^n), (\mathbf{v}_h, q_h)).$$

The second term in (3.8) corresponds to the so-called Temam's trick, which copes with the fact that the discrete fluid velocities are not divergence free. The third term is a weakly consistent stabilization term which allows to control the energy contributions of the convective term (first term of (3.8)) induced by the fact that

$$\hat{\mathbf{u}}_h^{n-1}|_\Sigma \neq \mathbf{w}_h^n|_\Sigma = \hat{\mathbf{d}}_h^{n-\frac{1}{2}}|_\Sigma.$$

166 Following [25, Chapter 5], we introduce a second weakly consistent stabilization term,
 167 namely,

$$(3.9) \quad s_{\Omega^{f,n}}(\mathbf{u}_h^n, \mathbf{v}_h) \stackrel{\text{def}}{=} -\frac{\rho^f}{2\tau} \left(\int_{\Omega^{f,n}} \mathbf{u}_h^n \cdot \mathbf{v}_h - \int_{\Omega^{f,n-1}} \mathbf{u}_h^n \cdot \mathbf{v}_h \right) + \frac{\rho^f}{2} \int_{\Omega^{f,n}} (\text{div } \mathbf{w}_h^n) \mathbf{u}_h^n \cdot \mathbf{v}_h,$$

whose purpose is to cope with the issues related to the so-called discrete geometric conservation law (see, e.g., [13]). Note that the weak consistency of (3.9) is a consequence of the Reynolds transport formula:

$$\frac{d}{dt} \int_{\Omega^f(t)} q = \int_{\Omega^f(t)} q \text{div } \mathbf{w}$$

for any smooth enough field $\hat{q} : \Omega^f \rightarrow \mathbb{R}^+$. Finally, the non-negative bi-linear term,

$$s_h^f(\mathbf{u}_h^{n-1}, \mathbf{w}_h^n; (\mathbf{u}_h^n, p_h^n), (\mathbf{v}_h, q_h)),$$

Algorithm 3.1 Explicit Robin-Robin scheme (fully discrete)

Assume \mathbf{u}_h^0 , \mathbf{d}_h^0 and $\mathbf{d}_h^{f,0}$, $\boldsymbol{\lambda}_h^0$ to be given and, for $n \geq 1$, perform:

- Solve solid: find $(\mathbf{d}_h^n, \dot{\mathbf{d}}_h^n) \in \mathbf{V}_h^s \times \mathbf{V}_h^s$, with $\dot{\mathbf{d}}_h^{n-\frac{1}{2}} = \partial_\tau \mathbf{d}_h^n$ such that

$$(3.10) \quad \rho^s \int_{\Omega^s} \partial_\tau \dot{\mathbf{d}}_h^n \cdot \boldsymbol{\xi}_h + \int_{\Omega^s} \bar{\boldsymbol{\Sigma}}_h^{n-\frac{1}{2}} : \partial_d (\mathbf{E}_h^{n-\frac{1}{2}}) \boldsymbol{\xi}_h + \alpha \int_\Sigma (\dot{\mathbf{d}}_h^{n-\frac{1}{2}} - \hat{\mathbf{u}}_h^{n-1}) \cdot \boldsymbol{\xi}_h \\ = - \int_\Sigma \boldsymbol{\lambda}_h^{n-1} \cdot \boldsymbol{\xi}_h$$

for all $\boldsymbol{\xi}_h \in \mathbf{V}_h^s$.

- Update fluid domain:

$$\mathbf{d}_h^{f,n} = \mathcal{L}_h(\mathbf{d}_h^n|_\Sigma), \quad \mathbf{w}_h^n = \partial_\tau \mathbf{d}_h^{f,n}, \quad \mathcal{A}_h^n = \mathbf{I}_{\Omega^f} + \mathbf{d}_h^{f,n}, \quad \Omega^{f,n} = \mathcal{A}_h^n(\Omega^f).$$

- Solve fluid: find $(\hat{\mathbf{u}}_h^n, \hat{p}_h^n) \in \mathbf{V}_h^f \times Q_h$ such that

$$(3.11) \quad \frac{\rho^f}{\tau} \left(\int_{\Omega^{f,n}} \mathbf{u}_h^n \cdot \mathbf{v}_h - \int_{\Omega^{f,n-1}} \mathbf{u}_h^{n-1} \cdot \mathbf{v}_h \right) - \rho^f \int_{\Omega^{f,n}} (\operatorname{div} \mathbf{w}_h^n) \mathbf{u}_h^n \cdot \mathbf{v}_h \\ + s_{\Omega^{f,n}}(\mathbf{u}_h^n, \mathbf{v}_h) + a_{\Omega^{f,n}}(\mathbf{u}_h^{n-1}, \mathbf{w}_h^n; (\mathbf{u}_h^n, p_h^n), (\mathbf{v}_h, q_h)) \\ + \alpha \int_\Sigma (\hat{\mathbf{u}}_h^n - \dot{\mathbf{d}}_h^{n-\frac{1}{2}}) \cdot \hat{\mathbf{v}}_h = \int_\Sigma \boldsymbol{\lambda}_h^{n-1} \cdot \hat{\mathbf{v}}_h$$

for all $(\hat{\mathbf{v}}_h, \hat{q}_h) \in \mathbf{V}_h^f \times Q_h$.

- Fluid-stress update: set $\boldsymbol{\lambda}_h^n \in \mathbf{V}_h^g$ as

$$(3.12) \quad \boldsymbol{\lambda}_h^n = \boldsymbol{\lambda}_h^{n-1} + \alpha (\dot{\mathbf{d}}_h^{n-\frac{1}{2}} - \hat{\mathbf{u}}_h^n) \quad \text{on } \Sigma.$$

169 stands for any given velocity and pressure stabilization operator (see, e.g., [26, 10]),
 170 whose purpose is to circumvent the issues related to the lack of robustness for both
 171 high local Reynolds numbers and the lack of inf-sup stability for the pair \mathbf{V}_h^f/M^f .

172 With all the above ingredients, the proposed fully discrete counterpart of (3.2)–
 173 (3.4) is detailed in Algorithm 3.1.

174 Some remarks are now in order. The relation (3.12) in Algorithm 3.1 is essentially
 175 a rewriting of (3.6)₂, in which the intermediate variable $\boldsymbol{\lambda}_h^n$ represents the discrete
 176 counterpart of the interfacial fluid stress on the reference configuration $\boldsymbol{\lambda}^n$, given by
 177 (3.1). Indeed, by combining (3.11) and (3.12), the update of the fluid-stress in the
 178 fourth step of Algorithm 3.1 can be formulated, in a more standard form as a fluid
 179 variational residual (see, e.g., [14]):

$$180 \quad (3.13) \quad \int_\Sigma \boldsymbol{\lambda}_h^n \cdot \boldsymbol{\mu}_h = \frac{\rho^f}{\tau} \left(\int_{\Omega^{f,n}} \mathbf{u}_h^n \cdot \mathcal{L}_h^f \boldsymbol{\mu}_h - \int_{\Omega^{f,n-1}} \mathbf{u}_h^{n-1} \cdot \mathcal{L}_h^f \boldsymbol{\mu}_h \right) \\ 181 \quad - \rho^f \int_{\Omega^{f,n}} (\operatorname{div} \mathbf{w}_h^n) \mathbf{u}_h^n \cdot \mathcal{L}_h^f \boldsymbol{\mu}_h + a_{\Omega^{f,n}}(\mathbf{u}_h^{n-1}, \mathbf{w}_h^n; (\mathbf{u}_h^n, p_h^n), (\mathcal{L}_h^f \boldsymbol{\mu}_h, 0))$$

for all $\boldsymbol{\mu}_h \in \mathbf{V}_h^g$ and where $\mathcal{L}_h^f : \mathbf{V}_h^g \rightarrow \mathbf{V}_h^f$ represents a linear fluid-sided lifting operator, such that, the nodal values of $\mathcal{L}_h^f \boldsymbol{\mu}_h$ vanish out of Σ and $(\mathcal{L}_h^f \boldsymbol{\mu}_h)|_\Sigma = \boldsymbol{\mu}_h$,

for all $\boldsymbol{\mu}_h \in \mathbf{V}_h^g$. We can hence see that, as indicated above, $\boldsymbol{\lambda}_h^n$ is nothing but the discrete counterpart of the interfacial fluid stress on the reference configuration. It is worth noting that the interfacial stabilization term in (3.8) introduces a weakly consistent perturbation of the fluid stresses approximation provided by (3.13). Indeed, this relation formally writes

$$\int_{\Sigma} \boldsymbol{\lambda}_h^n \cdot \boldsymbol{\mu}_h \equiv \int_{\Sigma^n} \boldsymbol{\sigma}(\mathbf{u}_h^n, p_h^n) \mathbf{n}_h \cdot \boldsymbol{\mu}_h - \frac{\rho^f}{2} \int_{\Sigma^n} (\mathbf{u}_h^{n-1} - \dot{\mathbf{d}}_h^{n-\frac{1}{2}} \circ (\mathcal{A}_h^n)^{-1}) \cdot \mathbf{n}_h (\mathbf{u}_h^n \cdot \boldsymbol{\mu}_h)$$

for all $\boldsymbol{\mu} \in \mathbf{V}_h^g$, or point-wise

$$\boldsymbol{\lambda}^n \equiv J^n \widehat{\boldsymbol{\sigma}}(\mathbf{u}^n, p^n) (\mathbf{F}^n)^{-T} \widehat{\mathbf{n}} - \frac{\rho^f J^n}{2} (\widehat{\mathbf{u}}^{n-1} - \dot{\mathbf{d}}^{n-\frac{1}{2}}) \cdot ((\mathbf{F}^n)^{-T} \widehat{\mathbf{n}}) \widehat{\mathbf{u}}^n \quad \text{on } \Sigma.$$

182 It should also be noted that these last two expressions are merely formal and, there-
183 fore, can not be used in the energy stability analysis of Algorithm 3.1, presented in
184 Section 3.1 below.

185 Algorithm 3.1 shares some similarities with the time-semidiscrete Robin-Robin
186 scheme proposed in [24], but with several fundamental differences. First, the method
187 is here formulated in a fully discrete setting, with a rigorous definition of the interfacial
188 fluid-stresses. Second, a suitable interfacial stabilization is added to control the energy
189 contributions of the convective term. This avoids the artificial modifications of the
190 fluid velocity on the interface advocated in [24, Section 3]. Third, the stability of the
191 method reported in the next paragraph also holds in 3D, irrespectively of the discrete
192 geometric conservation law, via the stabilization term (3.9). Finally, the stability
193 analysis (Section 3.1) and the numerical examples (of Section 5) cover the case of the
194 coupling with a general non-linear solid model.

195 **3.1. Energy stability analysis.** For $n \geq 1$, let the discrete energy and dissi-
196 pation be respectively defined as

$$E_h^n \stackrel{\text{def}}{=} \frac{\rho^f}{2} \|\mathbf{u}_h^n\|_{0, \Omega^f, n}^2 + \frac{\rho^s}{2} \|\dot{\mathbf{d}}_h^n\|_{0, \Omega^s}^2 + \int_{\Omega^s} W(\mathbf{E}_h^n) + \frac{\tau}{2} \left(\alpha \|\widehat{\mathbf{u}}_h^n\|_{0, \Sigma}^2 + \frac{1}{\alpha} \|\boldsymbol{\lambda}_h^n\|_{0, \Sigma}^2 \right),$$

$$G_h^n \stackrel{\text{def}}{=} \sum_{m=1}^n \tau \left(2\mu \|\boldsymbol{\epsilon}(\mathbf{u}_h^m)\|_{0, \Omega^f, m}^2 + \alpha \|\dot{\mathbf{d}}_h^{m-\frac{1}{2}} - \widehat{\mathbf{u}}_h^{m-1}\|_{0, \Sigma}^2 \right).$$

197 **THEOREM 1.** Let $\{(\widehat{\mathbf{u}}^n, \widehat{p}^n, \mathbf{d}^n, \dot{\mathbf{d}}^n, \boldsymbol{\lambda}^n)\}_{n \geq 1}$ be given by Algorithm 3.1. The follow-
198 ing energy estimate holds for $n \geq 1$

$$199 \quad (3.14) \quad E_h^n + G_h^n \leq E_h^0.$$

200 As a result, Algorithm 3.1 is unconditionally stable in the energy norm.

201 *Proof.* We proceed by testing (3.10) with $\boldsymbol{\xi}_h = \dot{\mathbf{d}}_h^{n-\frac{1}{2}}$ and (3.11) with $(\widehat{\mathbf{v}}_h, \widehat{q}_h) =$
202 $(\widehat{\mathbf{u}}_h^n, \widehat{p}_h^n)$. For the solid, we get

$$203 \quad (3.15) \quad \frac{\rho^s}{2} \partial_{\tau} \|\dot{\mathbf{d}}_h^n\|_{0, \Omega^s}^2 + \int_{\Omega^s} \overline{\boldsymbol{\Sigma}}_h^{n-\frac{1}{2}} : \partial_{\mathbf{d}} (\mathbf{E}_h^{n-\frac{1}{2}}) \dot{\mathbf{d}}_h^{n-\frac{1}{2}} + \alpha \int_{\Sigma} (\dot{\mathbf{d}}_h^{n-\frac{1}{2}} - \widehat{\mathbf{u}}_h^{n-1}) \cdot \dot{\mathbf{d}}_h^{n-\frac{1}{2}}$$

$$204 \quad \quad \quad = - \int_{\Sigma} \boldsymbol{\lambda}_h^{n-1} \cdot \dot{\mathbf{d}}_h^{n-\frac{1}{2}}.$$

From (2.5), we have

$$\begin{aligned} \partial_d(\mathbf{E}_h^{n-\frac{1}{2}})\dot{\mathbf{d}}_h^{n-\frac{1}{2}} &= \frac{1}{2} \left((\mathbf{F}_h^{s,n-\frac{1}{2}})^\top \partial_\tau \mathbf{F}_h^{s,n} + (\partial_\tau \mathbf{F}_h^{s,n})^\top \mathbf{F}_h^{s,n-\frac{1}{2}} \right) \\ &= \frac{1}{2\tau} \left((\mathbf{F}_h^{s,n})^\top \mathbf{F}_h^{s,n} - (\mathbf{F}_h^{s,n-1})^\top \mathbf{F}_h^{s,n-1} \right) \\ &= \partial_\tau \mathbf{E}_h^n. \end{aligned}$$

205 So that, by inserting the previous relation into (3.15) and using the definition of the
206 stress correction (3.5), we have

$$207 \quad (3.16) \quad \int_{\Omega^s} \bar{\Sigma}_h^{n-\frac{1}{2}} : \partial_\tau \mathbf{E}_h^n = \int_{\Omega^s} \partial_\tau W(\mathbf{E}_h^n).$$

208 By inserting (3.16) into (3.15), we ultimately arrive at:

$$209 \quad (3.17) \quad \frac{\rho^s}{2} \partial_\tau \|\dot{\mathbf{d}}_h^n\|_{0,\Omega^s}^2 + \partial_\tau \int_{\Omega^s} W(\mathbf{E}_h^n) + \alpha \int_{\Sigma} (\dot{\mathbf{d}}_h^{n-\frac{1}{2}} - \hat{\mathbf{u}}_h^{n-1}) \cdot \dot{\mathbf{d}}_h^{n-\frac{1}{2}} = - \int_{\Sigma} \lambda_h^{n-1} \cdot \dot{\mathbf{d}}_h^{n-\frac{1}{2}}.$$

210 For the fluid, the bulk terms are treated in a standard fashion (see [17, Proposi-
211 tion 9.4] and [25, Chapter 5]) with the sole differences in the control of the ALE time
212 derivative and of the convective terms, with the considered stabilizations. Using inte-
213 gration by parts, the fact that (by construction) $\mathbf{w}_h^n|_{\Sigma} = \dot{\mathbf{d}}_h^{n-\frac{1}{2}}|_{\Sigma}$ and the positiveness
214 of s_h^f , we have

$$\begin{aligned} 215 \quad (3.18) \quad a_{\Omega^f,n}(\mathbf{u}_h^{n-1}, \mathbf{w}_h^n; (\mathbf{u}_h^n, p_h^n), (\mathbf{u}_h^n, p_h^n)) &\geq 2\mu \|\epsilon(\mathbf{u}_h^n)\|_{0,\Omega^f,n}^2 \\ 216 \quad &+ \frac{\rho^f}{2} \int_{\Omega^f,n} (\mathbf{u}_h^{n-1} - \mathbf{w}_h^n) \cdot \nabla |\mathbf{u}_h^n|^2 + \frac{\rho^f}{2} \int_{\Omega^f,n} (\operatorname{div} \mathbf{u}_h^{n-1}) |\mathbf{u}_h^n|^2 \\ 217 \quad &- \frac{\rho^f}{2} \int_{\Sigma^n} (\mathbf{u}_h^{n-1} - \dot{\mathbf{d}}_h^{n-\frac{1}{2}}) \cdot \mathbf{n} |\mathbf{u}_h^n|^2 \\ 218 \quad &= 2\mu \|\epsilon(\mathbf{u}_h^n)\|_{0,\Omega^f,n}^2 + \frac{\rho^f}{2} \int_{\Omega^f,n} (\operatorname{div} \mathbf{w}_h^n) |\mathbf{u}_h^n|^2. \end{aligned}$$

219 Using (3.12) and the arguments reported in [17, Proposition 9.4] and [25, Chapter 5],
220 we finally obtain

$$\begin{aligned} 221 \quad (3.19) \quad \frac{\rho^f}{2} \partial_\tau \|\mathbf{u}_h^n\|_{0,\Omega^f,n}^2 + 2\mu \|\epsilon(\mathbf{u}_h^n)\|_{0,\Omega^f,n}^2 &\leq \int_{\Sigma} \lambda_h^{n-1} \cdot \hat{\mathbf{u}}_h^n - \alpha \int_{\Sigma} (\hat{\mathbf{u}}_h^n - \dot{\mathbf{d}}_h^{n-\frac{1}{2}}) \cdot \hat{\mathbf{u}}_h^n \\ 222 \quad &= \int_{\Sigma} \lambda_h^n \cdot \hat{\mathbf{u}}_h^n. \end{aligned}$$

223 Next, we proceed to add the energy contributions of the solid, as given by (3.17),
224 and the fluid, as expressed in (3.19). This results in the following energy expression:

$$225 \quad (3.20) \quad \frac{\rho^f}{2} \partial_\tau \|\mathbf{u}_h^n\|_{0,\Omega^f,n}^2 + \frac{\rho^s}{2} \partial_\tau \|\dot{\mathbf{d}}_h^n\|_{0,\Omega^s}^2 + \partial_\tau \int_{\Omega^s} W(\mathbf{E}_h^n) + 2\mu \|\epsilon(\mathbf{u}_h^n)\|_{0,\Omega^f,n}^2 \leq R_h^n,$$

where

$$R_h^n \stackrel{\text{def}}{=} \alpha \int_{\Sigma} (\hat{\mathbf{u}}_h^{n-1} - \dot{\mathbf{d}}_h^{n-\frac{1}{2}}) \cdot \dot{\mathbf{d}}_h^{n-\frac{1}{2}} - \int_{\Sigma} \lambda_h^{n-1} \cdot \dot{\mathbf{d}}_h^{n-\frac{1}{2}} + \int_{\Sigma} \lambda_h^n \cdot \hat{\mathbf{u}}_h^n.$$

226 We can now proceed as in the case with a fixed domain [5], which yields

$$227 \quad (3.21) \quad R_h^n = \frac{\alpha}{2} (\|\widehat{\mathbf{u}}_h^{n-1}\|_{0,\Sigma}^2 - \|\widehat{\mathbf{u}}_h^n\|_{0,\Sigma}^2) + \frac{1}{2\alpha} (\|\boldsymbol{\lambda}_h^{n-1}\|_{0,\Sigma}^2 - \|\boldsymbol{\lambda}_h^n\|_{0,\Sigma}^2) - \alpha \|\dot{\mathbf{d}}_h^{n-\frac{1}{2}} - \widehat{\mathbf{u}}_h^{n-1}\|_{0,\Sigma}^2,$$

228 Finally, by inserting (3.21) into (3.20), we obtain

$$229 \quad \frac{\rho^f}{2} \partial_\tau \|\mathbf{u}_h^n\|_{0,\Omega^f,n}^2 + \frac{\rho^s}{2} \partial_\tau \|\dot{\mathbf{d}}_h^n\|_{0,\Omega^s}^2 + \partial_\tau \int_{\Omega^s} W(\mathbf{E}_h^n) + 2\mu \|\boldsymbol{\epsilon}(\mathbf{u}_h^n)\|_{0,\Omega^f,n}^2 \\ 230 \quad + \frac{\alpha}{2} \|\widehat{\mathbf{u}}_h^n\|_{0,\Sigma}^2 + \frac{\tau}{2\alpha} \|\boldsymbol{\lambda}_h^n\|_{0,\Sigma}^2 + \alpha \|\dot{\mathbf{d}}_h^{n-\frac{1}{2}} - \widehat{\mathbf{u}}_h^{n-1}\|_{0,\Sigma}^2 \leq \frac{\alpha}{2} \|\widehat{\mathbf{u}}_h^{n-1}\|_{0,\Sigma}^2 + \frac{1}{2\alpha} \|\boldsymbol{\lambda}_h^{n-1}\|_{0,\Sigma}^2.$$

231 The energy estimate (3.14) then follows by multiplying the previous expression by τ
232 and then summing over $m = 1, \dots, n$, which completes the proof. \square

233 **4. Error estimate in a linearized setting.** In this section, we provide an
234 error analysis of Algorithm 3.1 in a simplified setting. To this purpose, we assume
235 that the solid undergoes infinitesimal displacements and that convective effects are
236 negligible in the fluid. Under these assumptions, the non-linear coupled problem (2.1)-
237 (2.3) can be replaced by the following linear Stokes-elasticity system in the reference
238 configuration $\Omega^f \cup \Omega^s$:

$$239 \quad (4.1) \quad \begin{cases} \rho^f \partial_t \mathbf{u} - \operatorname{div} \boldsymbol{\sigma}(\mathbf{u}, p) = \mathbf{0} & \text{in } \Omega^f \times (0, T), \\ \operatorname{div} \mathbf{u} = 0 & \text{in } \Omega^f \times (0, T), \\ \mathbf{u} = \mathbf{0} & \text{on } \Gamma^f \times (0, T), \end{cases}$$

$$240 \quad (4.2) \quad \begin{cases} \rho^s \partial_t \dot{\mathbf{d}} - \operatorname{div} \boldsymbol{\sigma}(\mathbf{d}) = \mathbf{0} & \text{in } \Omega^s \times (0, T), \\ \dot{\mathbf{d}} = \partial_t \mathbf{d} & \text{in } \Omega^s \times (0, T), \\ \mathbf{d} = \mathbf{0} & \text{on } \Gamma^s \times (0, T), \end{cases}$$

$$241 \quad (4.3) \quad \begin{cases} \mathbf{u} = \dot{\mathbf{d}} & \text{on } \Sigma \times (0, T), \\ \boldsymbol{\sigma}(\mathbf{u}, p) \mathbf{n} = \boldsymbol{\sigma}(\mathbf{d}) \mathbf{n} & \text{on } \Sigma \times (0, T), \end{cases}$$

complemented with the initial conditions: $\mathbf{d}(0, \cdot) = \mathbf{d}_0$, $\dot{\mathbf{d}}(0, \cdot) = \dot{\mathbf{d}}_0$ in Ω^s , and
 $\mathbf{u}(0, \cdot) = \mathbf{u}_0$ in Ω^f and where $T > 0$ denotes the final time. The symbol $\boldsymbol{\sigma}(\mathbf{d})$ stands
for the linearized solid stress tensor, which is assumed to be given in terms of the
solid displacement \mathbf{d} by the following relation:

$$\boldsymbol{\sigma}(\mathbf{d}) \stackrel{\text{def}}{=} 2L_1 \boldsymbol{\epsilon}(\mathbf{d}) + L_2 (\operatorname{div} \mathbf{d}) \mathbf{I},$$

242 where $L_1, L_2 > 0$ denote the so called Lamé coefficients of the solid.

243 Assuming that $\boldsymbol{\lambda} \in L^2(\Sigma)$, the solution of (4.1)–(4.3) satisfies the weak formula-
244 tion

$$245 \quad (4.4) \quad \begin{aligned} & \rho^s \int_{\Omega^s} \partial_t \dot{\mathbf{d}} \cdot \boldsymbol{\xi} + a^s(\mathbf{d}, \boldsymbol{\xi}) + \int_{\Sigma} \boldsymbol{\lambda} \cdot \boldsymbol{\xi} = 0, \\ & \int_{\Omega^s} \dot{\mathbf{d}} \cdot \boldsymbol{\phi} - \int_{\Omega^s} \partial_t \mathbf{d} \cdot \boldsymbol{\phi} = 0, \\ & \rho^f \int_{\Omega^f} \partial_\tau \mathbf{u} \cdot \mathbf{v} + a^f((\mathbf{u}, p), (\mathbf{v}, q)) - \int_{\Sigma} \boldsymbol{\lambda} \cdot \mathbf{v} = 0, \\ & \int_{\Sigma} (\mathbf{u} - \dot{\mathbf{d}}) \cdot \boldsymbol{\mu} = 0 \end{aligned}$$

246 for all $(\boldsymbol{\xi}, \boldsymbol{\phi}, \mathbf{v}, q) \in \mathbf{V}^s \times \mathbf{V}^s \times \mathbf{V}^f \times M^f$. Here, the bilinear forms of the fluid, denoted
 247 as a^f , and of the solid, denoted as a^s , are respectively given by

$$248 \quad a^f((\mathbf{u}, p), (\mathbf{v}, q)) \stackrel{\text{def}}{=} 2\mu \int_{\Omega^f} \boldsymbol{\epsilon}(\mathbf{u}) : \boldsymbol{\epsilon}(\mathbf{v}) - \int_{\Omega^f} p \operatorname{div} \mathbf{v} + \int_{\Omega^f} q \operatorname{div} \mathbf{u},$$

$$249 \quad a^s(\mathbf{d}, \boldsymbol{\xi}) \stackrel{\text{def}}{=} 2L_1 \int_{\Omega^s} \boldsymbol{\epsilon}(\mathbf{d}) : \boldsymbol{\epsilon}(\boldsymbol{\xi}) + L_2 \int_{\Omega^s} (\operatorname{div} \mathbf{d})(\operatorname{div} \boldsymbol{\xi}).$$

We also introduce the elastic energy norm of the solid given by the relation

$$\|\boldsymbol{\xi}\|_s \stackrel{\text{def}}{=} \sqrt{a^s(\boldsymbol{\xi}, \boldsymbol{\xi})}$$

250 for all $\boldsymbol{\xi} \in \mathbf{V}^s$.

251 For the numerical approximation of (4.4) we consider the Robin-Robin loosely
 252 coupled scheme introduced in [5] and detailed in Algorithm 4.1. As in Section 3, we
 253 employ a backward Euler method for the fluid and a mid-point scheme for the solid.
 254 In addition, for the spatial discretization, we consider a piecewise affine continuous
 255 finite elements, where we assume that the fluid and solid meshes are fitted. In other
 256 words, Algorithm 4.1 is essentially the linear counterpart of Algorithm 3.1. Here, we
 257 accommodate for the lack of inf-sup stability by using a pressure stabilized bilinear
 258 form for the fluid (see [4]),

$$259 \quad (4.5) \quad a_h^f((\mathbf{u}_h, p_h), (\mathbf{v}_h, q_h)) \stackrel{\text{def}}{=} a^f((\mathbf{u}_h, p_h), (\mathbf{v}_h, q_h)) + \frac{\gamma_p h^2}{\mu} \int_{\Omega^f} \nabla p_h \cdot \nabla q_h,$$

260 with $\gamma_p > 0$ a user-defined parameter.

Algorithm 4.1 Robin-based loosely coupled scheme (linear case).

Assume \mathbf{u}_h^0 , \mathbf{d}_h^0 and $\dot{\mathbf{d}}_h^{f,0}$, $\boldsymbol{\lambda}_h^0$ to be given and, for $n \geq 1$, perform:

1. Solid subproblem: Find $\dot{\mathbf{d}}_h^n, \mathbf{d}_h^n \in \mathbf{V}_h^s$ such that $\dot{\mathbf{d}}_h^{n-\frac{1}{2}} = \partial_\tau \mathbf{d}_h^n$ and

$$(4.6) \quad \rho^s \int_{\Omega^s} \partial_\tau \dot{\mathbf{d}}_h^n \cdot \boldsymbol{\xi}_h + a^s(\mathbf{d}_h^{n-\frac{1}{2}}, \boldsymbol{\xi}_h) + \alpha \int_\Sigma (\dot{\mathbf{d}}_h^{n-\frac{1}{2}} - \mathbf{u}_h^{n-1}) \cdot \boldsymbol{\xi}_h = - \int_\Sigma \boldsymbol{\lambda}_h^{n-1} \cdot \boldsymbol{\xi}_h$$

for all $\boldsymbol{\xi}_h \in \mathbf{V}_h^s$.

2. Fluid subproblem: Find $(\mathbf{u}_h^n, p_h^n) \in \mathbf{V}_h^f \times M_h^f$ such that

$$(4.7) \quad \rho^f \int_{\Omega^f} \partial_\tau \mathbf{u}_h^n \cdot \mathbf{v}_h + a_h^f((\mathbf{u}_h^n, p_h^n), (\mathbf{v}_h, q_h)) + \alpha \int_\Sigma (\mathbf{u}_h^n - \dot{\mathbf{d}}_h^{n-\frac{1}{2}}) \cdot \mathbf{v}_h = \int_\Sigma \boldsymbol{\lambda}_h^{n-1} \cdot \mathbf{v}_h$$

for all $(\mathbf{v}_h, q_h) \in \mathbf{V}_h^f \times M_h^f$.

3. Fluid-stress update: set $\boldsymbol{\lambda}_h^n \in \mathbf{V}_h^g$ as

$$(4.8) \quad \boldsymbol{\lambda}_h^n = \boldsymbol{\lambda}_h^{n-1} + \alpha (\dot{\mathbf{d}}_h^{n-\frac{1}{2}} - \mathbf{u}_h^n) \quad \text{on } \Sigma.$$

261 **4.1. Relation to previous results.** In [5], we proved that Algorithm 4.1 was
 262 optimal in space and sub-optimal in time, specifically $\mathcal{O}(h + \tau^{\frac{1}{2}})$. However, following
 263 new numerical experiments and the results of [6], it has become clear that the result

264 in [5] is not a strict bound. Following the techniques developed in [6], we are able
 265 to prove that the Robin-Robin scheme for the linear case is, in fact, nearly-optimal
 266 in time. This result is presented below, along with the main features of the analysis.
 267 The full analysis is covered in detail in [12, Chapter 5].

268 **4.2. Nearly-optimal error estimate.** In what follows, $N \in \mathbb{N}$ is such that
 269 $N\tau \leq T$ and let $\{(\mathbf{u}_h^n, p_h^n, \boldsymbol{\lambda}_h^n, \mathbf{d}_h^n, \dot{\mathbf{d}}_h^n)\}_{1 \leq n \leq N} \subset \mathbf{V}_h^f \times M_h^f \times \mathbf{V}_h^g \times \mathbf{V}_h^s \times \mathbf{V}_h^s$ be given
 270 by Algorithm 4.1. We introduce the discrete error terms

$$271 \quad \mathbf{e}_{\mathbf{d},h}^n \stackrel{\text{def}}{=} \mathbf{d}_h^n - R_h^s \mathbf{d}^n, \quad \dot{\mathbf{e}}_{\mathbf{d},h}^n \stackrel{\text{def}}{=} \dot{\mathbf{d}}_h^n - R_h^s \dot{\mathbf{d}}^n,$$

$$272 \quad \mathbf{e}_{\mathbf{u},h}^n \stackrel{\text{def}}{=} \mathbf{u}_h^n - R_h^f \mathbf{u}^n, \quad e_{p,h}^n \stackrel{\text{def}}{=} p_h^n - S_h p^n, \quad \mathbf{e}_{\boldsymbol{\lambda},h}^n \stackrel{\text{def}}{=} \boldsymbol{\lambda}_h^n - \pi_h \boldsymbol{\lambda}^n,$$

273 where $\boldsymbol{\lambda}^n = \boldsymbol{\sigma}(\mathbf{u}^n, p^n) \mathbf{n}$ on the interface Σ and where R_h^f, R_h^s respectively denote the
 274 Scott-Zhang interpolants (see, e.g., [23]) projecting onto the finite element spaces \mathbf{V}_h^s
 275 and \mathbf{V}_h^f , and S_h is the Scott-Zhang interpolant into M_h^f modified by a global constant
 276 so the average on Ω^f is zero. For projecting into \mathbf{V}_h^g , we use the notation π_h , the L^2
 277 orthogonal projection from \mathbf{V}^g to \mathbf{V}_h^g . We employ the Scott-Zhang interpolant for this
 278 analysis because it allows significant flexibility when selecting the degrees of freedom.
 279 Indeed, we may choose the degrees of freedom so that we will have $R_h^s \mathbf{v} = R_h^f \mathbf{w}$ on Σ
 280 if $\mathbf{v} \in [H^1(\Omega^s)]^2$ and $\mathbf{w} \in [H^1(\Omega^f)]^2$ and $\mathbf{v} = \mathbf{w}$ on Σ .

281 We may then define the following quantities to construct our error estimate:

$$282 \quad \mathcal{S}_h^n \stackrel{\text{def}}{=} \|\mathbf{e}_{\mathbf{d},h}^n\|_s^2 + \rho^s \|\mathbf{e}_{\mathbf{d},h}^n\|_{0,\Omega^s}^2 + \rho^f \|\mathbf{e}_{\mathbf{u},h}^n\|_{0,\Omega^f}^2,$$

$$283 \quad \mathcal{E}_h^n \stackrel{\text{def}}{=} \tau \alpha \|\mathbf{e}_{\mathbf{u},h}^n\|_{0,\Sigma}^2 + \frac{\tau}{\alpha} \|\mathbf{e}_{\boldsymbol{\lambda},h}^n\|_{0,\Sigma}^2,$$

$$284 \quad \mathcal{W}_h^n \stackrel{\text{def}}{=} \rho^f \|\mathbf{e}_{\mathbf{u},h}^n - \mathbf{e}_{\mathbf{u},h}^{n-1}\|_{0,\Omega^f}^2 + 4\mu\tau \|\boldsymbol{\varepsilon}(\mathbf{e}_{\mathbf{u},h}^n)\|_{0,\Omega^f}^2 + 2\tau h^2 \|\nabla e_{p,h}^n\|_{0,\Omega^s}^2,$$

$$285 \quad \mathcal{Z}_h^n \stackrel{\text{def}}{=} \tau \alpha \|\mathbf{e}_{\mathbf{d},h}^{n-\frac{1}{2}} - \mathbf{e}_{\mathbf{u},h}^{n-1}\|_{0,\Sigma}^2$$

286 for $1 \leq n \leq N$. Finally, as described in [12, Chapter 5], the quasi-optimal error result
 287 requires two key assumptions, which we state here. The motivation behind these
 288 assumptions will be explained further below. First, we assume that the normal \mathbf{n}^s
 289 can be extended from Σ into Ω^s in such a way that its gradient is bounded.

290 **ASSUMPTION 1.** *There exists $\tilde{\mathbf{n}}^s \in [\mathbf{W}^{1,\infty}(\Omega^s)]^2$ such that $\tilde{\mathbf{n}}^s|_{\Sigma} = \mathbf{n}^s$.*

291 The second assumption is the existence of a function $\tilde{\phi} : \Omega^s \rightarrow \mathbb{R}$ that serves as a
 292 pseudo-lifting operator from the interface Σ into the interior of the solid domain Ω^s .

293 **ASSUMPTION 2.** *Assume that $\tau < \frac{1}{2}$. There exists a function $\tilde{\phi} : \Omega^s \rightarrow \mathbb{R}$ satisfy-*
 294 *ing:*

- 295 (i) $0 \leq \tilde{\phi} \leq 1$;
- 296 (ii) $\tilde{\phi} \in \mathbf{V}^s$;
- 297 (iii) $|\{x \in \Sigma : \tilde{\phi}(x) \neq 1\}| \leq C\tau$;
- 298 (iv) $\|\nabla \tilde{\phi}\|_{0,\Omega^s}^2 \leq C(1 + \log \frac{1}{\tau})$;

299 where each $C > 0$ represents a general constant independent of τ and of the physical
 300 parameters.

301 With these assumptions established, the quasi-optimal error results proceeds as
 302 follows.

303 THEOREM 2. Under Assumptions 1 and 2, and assuming that the solution is
 304 smooth enough so that Y_h defined below and $\|\varepsilon(\dot{\mathbf{d}})\|_{L^2(0,T;L^\infty(\Omega^s))}^2$, $\|\operatorname{div} \dot{\mathbf{d}}\|_{L^2(0,T;L^\infty(\Omega^s))}^2$
 305 are bounded, we have the following bound on the discrete error

$$306 \quad (4.9) \quad \max_{1 \leq m \leq n} \{\mathcal{S}_h^m + \mathcal{E}_h^m\} + \sum_{m=1}^n (\mathcal{Z}_h^m + \mathcal{W}_h^m)$$

$$307 \quad \leq C\tau^2 \left[\frac{(1+T)(L_1+L_2)^3}{\alpha^2} \left((1+\log \tau^{-1}) \|\varepsilon(\dot{\mathbf{d}})\|_{L^2(0,T;L^\infty(\Omega^s))}^2 \right. \right.$$

$$308 \quad \left. \left. + \|\operatorname{div} \dot{\mathbf{d}}\|_{L^2(0,T;L^\infty(\Omega^s))}^2 \right) + Y_h \right],$$

309 where $Y_h \stackrel{\text{def}}{=} \sum_{i=1}^3 Y_{i,h}$ is given by

$$310 \quad Y_{1,h} \stackrel{\text{def}}{=} h^2 \left[(1+h^2)\rho^s(1+T)\|\partial_t \dot{\mathbf{d}}\|_{L^2(0,T;H^2(\Omega^s))}^2 + (1+h^2)\rho^f T \|\partial_t \mathbf{u}\|_{L^2(0,T;H^2(\Omega^f))}^2 \right.$$

$$311 \quad \left. + (1+T)(L_1+L_2)\|\dot{\mathbf{d}}\|_{L^2(0,T;H^2(\Omega^s))}^2 + \mu \|\mathbf{u}\|_{L^2(0,T;H^2(\Omega^f))}^2 \right.$$

$$312 \quad \left. + \frac{h^2}{\mu} \|p\|_{L^2(0,T;H^2(\Omega^f))}^2 + (L_1+L_2)\|\mathbf{d}\|_{L^2(0,T;H^2(\Omega^s))}^2 \right.$$

$$313 \quad \left. + (L_1+L_2)\|\mathbf{d}\|_{L^\infty(0,T;H^2(\Omega^s))}^2 \right] + \tau^2 \left[\tau^2 \rho^s(1+T)\|\partial_t^3 \dot{\mathbf{d}}\|_{L^2(0,T;L^2(\Omega^s))}^2 \right.$$

$$314 \quad \left. + \rho^f T \|\partial_t^2 \mathbf{u}\|_{L^2(0,T;L^2(\Omega^f))}^2 + \frac{h^4}{\mu} \|\partial_t p\|_{L^2(0,T;H^2(\Omega^f))}^2 \right.$$

$$315 \quad \left. + h^2(L_1+L_2)\|\dot{\mathbf{d}}\|_{L^2(0,T;H^2(\Omega^s))}^2 + h^2 \mu \|\partial_t \mathbf{u}\|_{L^2(0,T;H^2(\Omega^f))}^2 \right],$$

$$317 \quad Y_{2,h} \stackrel{\text{def}}{=} \tau^2 \left[(\tau^2)(1+T)(L_1+L_2)\|\partial_t^3 \dot{\mathbf{d}}\|_{L^2(0,T;H^1(\Omega^s))}^2 + h^2 \|\partial_t \mathbf{u}\|_{L^2(0,T;H^3(\Omega^f))}^2 \right.$$

$$318 \quad \left. + \left(1 + \alpha + \frac{\alpha^2}{\mu} + \mu + \mu^2 + \frac{(1+T)\mu^2}{\alpha} \right) \|\partial_t \mathbf{u}\|_{L^2(0,T;H^2(\Sigma))}^2 \right.$$

$$319 \quad \left. + (1+\alpha)\|\partial_t \dot{\mathbf{d}}\|_{L^2(0,T;L^2(\Sigma))}^2 + \left(1 + \frac{1+T}{\alpha} + \frac{1}{\mu} \right) \|\partial_t p\|_{L^2(0,T;L^2(\Sigma))}^2 \right.$$

$$320 \quad \left. + \tau^2(1+\alpha)\|\partial_t^3 \dot{\mathbf{d}}\|_{L^2(0,T;L^2(\Sigma))}^2 + T\rho^s \|\partial_t^2 \dot{\mathbf{d}}\|_{L^2(0,T;L^2(\Omega^s))}^2 \right.$$

$$321 \quad \left. + ((1+T)(L_1+L_2) + \rho^s)\|\partial_t \dot{\mathbf{d}}\|_{L^2(0,T;H^1(\Omega^s))}^2 + \frac{\mu^2 T}{\alpha} \|\varepsilon(\partial_t \mathbf{u})\|_{L^2(0,T;L^\infty(\Sigma))}^2 \right.$$

$$322 \quad \left. + \frac{T}{\alpha} \|\partial_t p\|_{L^2(0,T;L^\infty(\Sigma))}^2 + \rho^s \|\partial_t \dot{\mathbf{d}}\|_{L^\infty(0,T;L^2(\Omega^s))}^2 + h^2 \|\partial_t p\|_{L^2(0,T;H^1(\Omega^f))}^2 \right]$$

$$323 \quad + h^2 (\|\mathbf{u}\|_{L^2(0,T;H^3(\Omega^f))}^2 + \|\nabla p\|_{L^2(0,T;L^2(\Omega^f))}^2)$$

$$324 \quad + h^4 \left(\frac{T\mu^2}{\alpha} \|\partial_t \mathbf{u}\|_{L^2(0,T;H^2(\Sigma))}^2 + \frac{T}{\alpha} \|\partial_t p\|_{L^2(0,T;H^1(\Sigma))}^2 \right),$$

$$325 \quad Y_{3,h} \stackrel{\text{def}}{=} \tau^2 \left[\frac{(1+T)(L_1+L_2)^3 + \rho^s(L_1^2+L_2^2)}{\alpha^2} \|\dot{\mathbf{d}}\|_{L^2(0,T;H^2(\Omega^s))}^2 \right.$$

$$326 \quad \left. \right]$$

$$327 \quad + \frac{\rho^s T(L_1^2 + L_2^2)}{\alpha^2} \|\partial_t \dot{\mathbf{d}}\|_{L^2(0,T;H^2(\Omega^s))}^2 + \frac{\rho^s(L_1^2 + L_2^2)}{\alpha^2} \|\dot{\mathbf{d}}\|_{L^\infty(0,T;H^1(\Omega^s))}^2 \Big].$$

328 **4.3. Sketch of the proof to Theorem 2.** The proof of Theorem 2 is only
 329 sketched below due to the page limit, we refer to [12, Theorem 5.2.9] for full details.
 330 The argument consists of three parts. First, we begin with a preliminary bound.

LEMMA 4.1. *For $1 \leq n \leq N$, it holds*

$$\frac{3}{8} \max_{1 \leq m \leq n} \{S_h^m + \mathcal{E}_h^m\} + \frac{3}{8} \sum_{m=1}^n (\mathcal{W}_h^m + \mathcal{Z}_h^m) \leq \sum_{m=1}^n \frac{\tau}{\alpha} \int_{\Sigma} e_{\lambda,h}^{m-1} \cdot \mathbf{g}_{3,h}^m + CD_h^n,$$

where

$$\mathbf{g}_{3,h}^n \stackrel{\text{def}}{=} \frac{\alpha}{2} \mathbf{g}_{1,h}^n + \pi_h \mathbf{g}_2^n, \quad \mathbf{g}_{1,h}^n \stackrel{\text{def}}{=} R_h^f \mathbf{u}^n - R_h^f \mathbf{u}^{n-1}, \quad \mathbf{g}_2^n \stackrel{\text{def}}{=} \boldsymbol{\lambda}^n - \boldsymbol{\lambda}^{n-1}$$

331 and

$$332 \quad D_h^n \stackrel{\text{def}}{=} \tau \sum_{m=1}^{n-1} \left[\mu \|\varepsilon((R_h^f - I)\mathbf{u}^m)\|_{0,\Omega^f}^2 + \frac{1}{\mu} \|(S_h - I)p^m\|_{0,\Omega^f}^2 \right. \\
 333 \quad + (1+T) \|R_h^s \dot{\mathbf{d}}^{m-\frac{1}{2}} - \partial_\tau R_h^s \mathbf{d}_h^m\|_s^2 + (1+T) \|(R_h^s - I) \partial_\tau \mathbf{d}^m\|_s^2 + h^2 \|\mathbf{u}^m\|_{H^3(\Omega^f)}^2 \\
 334 \quad + (1+T) \|R_h^s \dot{\mathbf{d}}^{m-\frac{1}{2}} - \partial_\tau R_h^s \mathbf{d}_h^m\|_s^2 + (1+T) \|(R_h^s - I) \partial_\tau \mathbf{d}^m\|_s^2 + h^2 \|\mathbf{u}^m\|_{3,\Omega^f}^2 \\
 335 \quad + \left(\alpha + \frac{\alpha^2}{\mu} \right) \|\mathbf{g}_{1,h}^m\|_{0,\Sigma}^2 + \left(1 + \frac{1}{\alpha} + \frac{1}{\mu} \right) \|\boldsymbol{\lambda}^m - \boldsymbol{\lambda}^{m-1}\|_{0,\Sigma}^2 \\
 336 \quad + T \rho^s \|\partial_\tau R_h^s \dot{\mathbf{d}}^m - \partial_t \dot{\mathbf{d}}^{m-\frac{1}{2}}\|_{0,\Omega^s}^2 + \rho^f T \|\partial_\tau R_h^f \mathbf{u}^m - \partial_t \mathbf{u}^m\|_{0,\Omega^f}^2 \\
 337 \quad \left. + h^2 \|\nabla S_h p^m\|_{0,\Omega^f}^2 + \frac{\tau}{2\alpha} \|\mathbf{g}_{3,h}^m\|_{0,\Sigma}^2 \right] + \|(R_h^s - I) \mathbf{d}^n\|_s^2.$$

338 The proof of Lemma 4.1 requires some standard algebra along with Cauchy-Schwarz,
 339 Young's inequality, trace inequality, and Korn's inequality. A detailed proof is
 340 included in [12, Chapter 5]. The key takeaway, however, is that all of the terms in D_h^n
 341 are either the norms of splitting error terms such as $\mathbf{g}_{1,h}^n$ or interpolation errors such
 342 as $S_h p^n - p^n$. In both cases, the terms may be optimally bounded in terms of h and
 343 τ in the final step of the proof. However, the remaining unbounded term requires
 344 special care.

Consequently, the second part of the proof involves deriving a bound for the term

$$\sum_{m=1}^n \frac{\tau}{\alpha} \int_{\Sigma} e_{\lambda,h}^{m-1} \cdot \mathbf{g}_{3,h}^m.$$

345 If we attempt to bound this term by balancing $e_{\lambda,h}^{m-1}$ with terms appearing on the
 346 left-hand side of the estimate, we ultimately sacrifice a factor of $\tau^{\frac{1}{2}}$, resulting in
 347 suboptimal convergence, as done in [5]. Essentially, the challenge presented by this
 348 term is that it resides on the interface Σ , but to avoid a loss in accuracy we must
 349 somehow avoid the interface as much as possible.

350 To do this, we utilize the error equations of the solid to pull the term $e_{\lambda,h}^{n-1}$ from
 351 the interface Σ into the interior domain Ω^s . However, this requires us to construct

352 an extension of $\mathbf{g}_{3,h}^n$ into Ω^s which is in \mathbf{V}_h^s . Critically, this means that the extension
 353 needs to vanish on $\partial\Omega^s \setminus \Sigma$, which is not guaranteed for $\mathbf{g}_{3,h}^{n+1}$ due to the presence of
 354 the term $\pi_h(\boldsymbol{\lambda}^{n+1} - \boldsymbol{\lambda}^n)$. Therefore, we will utilize the extended normal $\tilde{\mathbf{n}}_s$ and the
 355 function $\tilde{\phi}$ defined in Assumptions 1 and 2 to construct a cut-off function technique
 356 to continuously lift the residual $\mathbf{g}_{3,h}^{n+1}$ from \mathbf{V}_h^g into \mathbf{V}_h^s .

357 The result of this extension step yields a quasi-optimal bound stated in the fol-
 358 lowing lemma.

LEMMA 4.2. *Under Assumptions 1 and 2 we have*

$$\frac{\tau}{\alpha} \sum_{m=1}^n \int_{\Sigma} \mathbf{e}_{\boldsymbol{\lambda},h}^{m-1} \cdot \mathbf{g}_{3,h}^m \leq \frac{1}{8} \max_{1 \leq m \leq n} \{S_h^m + \mathcal{E}_h^m\} + \frac{1}{8} \sum_{m=1}^n \mathcal{Z}_h^m + C\Psi_h^n,$$

359 where $\Psi_h^n \stackrel{\text{def}}{=} \Psi_{1,h}^n + \Psi_{2,h}^n$ given by

$$\begin{aligned} 360 \quad \Psi_1^n &\stackrel{\text{def}}{=} T\tau^3 \rho^s \sum_{m=1}^n \|\partial_{\tau}^2 R_h^s \dot{\mathbf{d}}^n\|_{0,\Omega^s}^2 + \rho^s \|\mathbf{g}_{1,h}^n\|_{0,\Omega^s}^2 \\ 361 \quad &+ \tau \sum_{m=1}^n \left[(1+T) \|\mathbf{g}_{1,h}^m\|_s^2 + (1+\alpha) \|\mathbf{g}_{1,h}^m\|_{0,\Sigma}^2 + \|\boldsymbol{\lambda}^m - \boldsymbol{\lambda}^{m-1}\|_{0,\Sigma}^2 \right. \\ 362 \quad &+ \rho^s \|\partial_{\tau} R_h^s \dot{\mathbf{d}}^m - \partial_t \dot{\mathbf{d}}^{m-\frac{1}{2}}\|_{0,\Omega^s}^2 + \rho^s \|\mathbf{g}_{1,h}^{n+1}\|_{0,\Omega^s}^2 + \|(R_h^s - I)\mathbf{d}^{m-\frac{1}{2}}\|_s^2 \\ 363 \quad &+ \alpha \|R_h^f \mathbf{u}^m - \partial_{\tau} R_h^s \mathbf{d}^m\|_{0,\Sigma}^2 + \alpha \|R_h^s \dot{\mathbf{d}}^{m-\frac{1}{2}} - \partial_{\tau} R_h^s \mathbf{d}^m\|_{0,\Sigma}^2 \left. \right], \end{aligned}$$

364

$$\begin{aligned} 365 \quad \Psi_2^n &\stackrel{\text{def}}{=} \frac{T\tau^3 \rho^s}{\alpha^2} \sum_{m=1}^n \|\partial_{\tau}^2 R_h^s (\tilde{\phi} \boldsymbol{\sigma}(\mathbf{d}^{m-1}) \tilde{\mathbf{n}}^s)\|_{0,\Omega^s}^2 + \frac{\rho^s}{\alpha^2} \|\tilde{\mathbf{g}}_{2,h}^n\|_{0,\Omega^s}^2 + \frac{Th^2}{\alpha} \sum_{m=1}^n \|\mathbf{g}_2^m\|_{1,\Sigma}^2 \\ 366 \quad &+ \tau \sum_{m=1}^n \left[\frac{1+T}{\alpha^2} \|\tilde{\mathbf{g}}_{2,h}^m\|_s^2 + \left(1 + \frac{1}{\alpha}\right) \|\boldsymbol{\lambda}^{n+1} - \boldsymbol{\lambda}^n\|_{0,\Sigma}^2 \right. \\ 367 \quad &+ \|\mathbf{g}_{1,h}^m\|_{0,\Sigma}^2 + \rho^s \|\partial_{\tau} R_h^s \dot{\mathbf{d}}^m - \partial_t \dot{\mathbf{d}}^{m-\frac{1}{2}}\|_{0,\Omega^s}^2 + \frac{\rho^s}{\alpha^2} \|\tilde{\mathbf{g}}_{2,h}^m\|_{0,\Omega^s}^2 \\ 368 \quad &+ \|(R_h^s - I)\mathbf{d}^{m-\frac{1}{2}}\|_s^2 + \|R_h^f \mathbf{u}^m - \partial_{\tau} R_h^s \mathbf{d}^m\|_{0,\Sigma}^2 \\ 369 \quad &+ \|R_h^s \dot{\mathbf{d}}^{m-\frac{1}{2}} - \partial_{\tau} R_h^s \mathbf{d}^m\|_{0,\Sigma}^2 + \frac{T}{\alpha} \|\mathbf{g}_2^m\|_{L^\infty(\Sigma)}^2 \left. \right]. \end{aligned}$$

370 Finally, in the third step of the proof, it remains to bound the terms D_h^n and Ψ_h^n ,
 371 which is the purpose of the next lemma.

372 LEMMA 4.3. *Under Assumptions 1 and 2, we have, for $1 \leq n \leq N$,*

$$\begin{aligned} 373 \quad D_h^n + \Psi_h^n &\leq C\tau^2 \left[\frac{(1+T)(L_1 + L_2)^3}{\alpha^2} \left((1 + \log \tau^{-1}) \|\boldsymbol{\varepsilon}(\dot{\mathbf{d}})\|_{L^2(0,T;L^\infty(\Omega^s))}^2 + \right. \right. \\ 374 \quad &\left. \left. \|\operatorname{div} \dot{\mathbf{d}}\|_{L^2(0,T;L^\infty(\Omega^s))}^2 \right) + CY_h \right]. \end{aligned}$$

375 The error estimate (4.9) then follows by combining the results of Lemmas 4.1–4.3.

376 **5. Numerical examples.** In this section, we illustrate the accuracy properties
 377 of Algorithms 3.1 in a series of well-known numerical examples.

378 **5.1. Convergence study in a simplified framework.** The objective of this
 379 first example is to provide numerical evidence of the nearly-optimal convergence result
 380 of Theorem 2. We will in particular investigate the effect on the accuracy of the solid
 381 parameters L_1, L_2 involved in the error estimate (4.9). To this purpose, we consider
 382 the pressure wave propagation benchmark of [16, Section 6.1.1] with the simplified
 383 coupled problem (4.1)-(4.3). We hence take $\Omega^f = [0, L] \times [0, R]$, $\Omega^s = [0, L] \times [R, R+\epsilon]$,
 384 with $L = 6$, $R = 0.5$ and $\epsilon = 0.1$. All the units are in the CGS system. At the fluid
 385 inlet boundary $x = 0$ a sinusoidal pressure of maximal amplitude $2 \cdot 10^4$ is enforced
 386 during $5 \cdot 10^{-3}$ second. Zero traction is prescribed at the outlet $x = 6$ and a symmetry
 387 condition is enforced on the lower wall. Transverse membrane effects are included in
 388 the solid equation (4.2)₁ through the additional zeroth-order term $c_0 \mathbf{d}$. The solid is
 389 clamped at its extremities and zero traction is enforced on its top boundary.

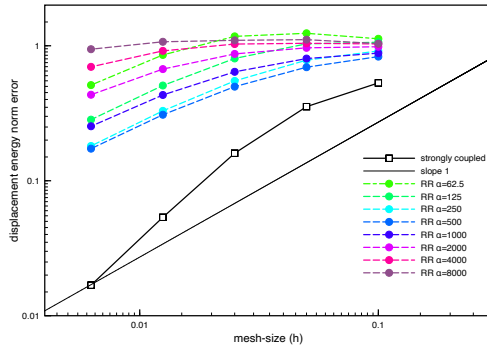


FIG. 1. Convergence histories for $E = 1.58 \cdot 10^6$.

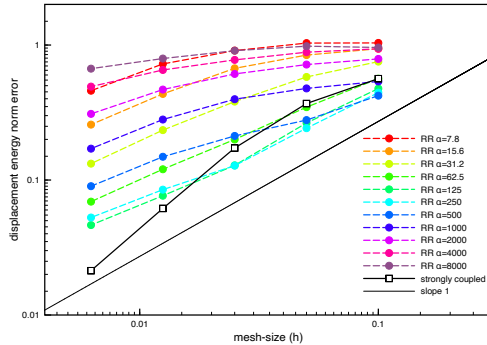
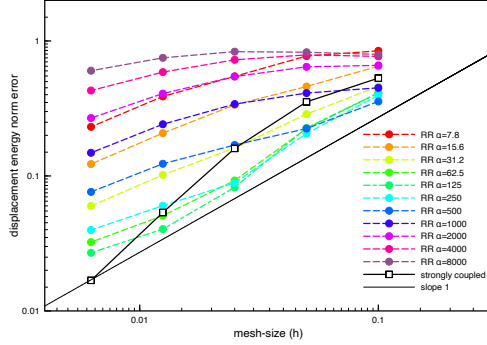


FIG. 2. Convergence histories for $E = 3.16 \cdot 10^5$.

390 The fluid and solid physical parameters are $\rho^f = 1$, $\mu = 0.035$, $\rho^s = 1.1$, $L_1 =$
 391 $1.15 \cdot 10^6$, $L_2 = 1.7 \cdot 10^6$ and $c_0 = 4 \cdot 10^6$. The pressure stabilization parameter in (4.5)
 392 is set to $\gamma_p = 10^{-3}$. All the computations have been carried out with the **FreeFem++**
 393 software (see [22]).

In order to illustrate the accuracy of Algorithm 4.1, we evaluate the relative displacement error $\|\mathbf{d}_h^N - \mathbf{d}(T)\|_e / \|\mathbf{d}(T)\|_e$ at the final time $T = 0.015$ for different


 FIG. 3. Convergence histories for $E = 1.58 \cdot 10^5$.

values of the discretization parameters under $\tau = \mathcal{O}(h)$, namely,

$$\tau \in \{5 \cdot 10^{-4} / 2^i\}_{i=0}^4, \quad h \in \{0.1 / 2^i\}_{i=0}^4.$$

394 The relative errors are calculated with a reference solution obtained with an implicit
 395 coupling scheme and a fine space-time grid ($h = 0.003125$ and $\tau = 10^{-6}$). The
 396 resulting convergence histories are reported in Figures 1–3 for three decreasing values
 397 of the Young modulus E . For comparison purposes, the results obtained with the
 398 implicit coupling scheme are also provided.

399 Several remarks are in order. The results indicate that there exists an optimal
 400 value of the Robin parameter α in terms of accuracy, and that accuracy tends to
 401 degrade for large or small values of α . Figures 1–3 also show that overall first-order
 402 accuracy $\mathcal{O}(h)$ is obtained for some values of α . This is more noticeable in Figures 2
 403 and 3. The results show that accuracy tends to degrade when increasing the elastic
 404 parameters L_1 and L_2 . All these observations are in agreement with the error estimate
 405 provided by Theorem 2. The results of Figures 1–3 indicate also that the optimal
 406 value of the Robin parameter α is proportional to \sqrt{E} . Such scaling equilibrates the
 407 contributions of the error bound provided by Theorem 2, which suggests the choice
 408 $\alpha = \gamma \sqrt{\rho^s E}$, with γ a user-defined dimensionless parameter.

409 **5.2. Lid-driven cavity with flexible bottom.** As second numerical example,
 410 we consider the classical shear-driven cavity problem with a flexible bottom (see, e.g.,
 411 [19]). The fluid domain is the unit square $\Omega^f = [0, 1] \times [0, 1]$ with the fluid-solid
 412 interface on the lower boundary $\Sigma = [0, 1] \times \{0\}$. All the units are given in the SI
 413 system.

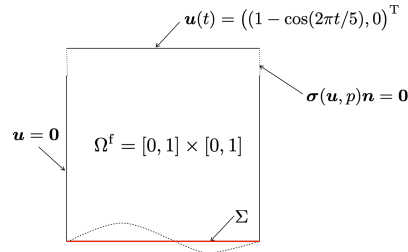


FIG. 4. Geometric description.

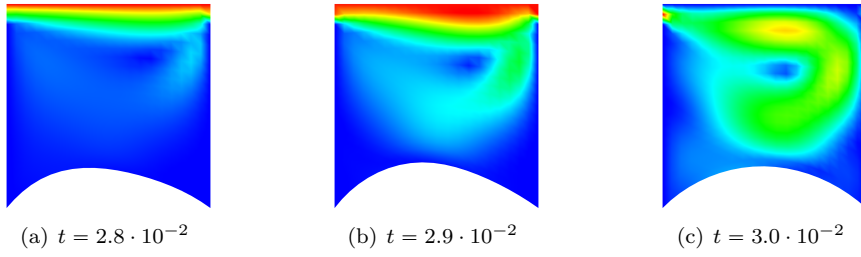


FIG. 5. Snapshots of the fluid velocity in the deformed configuration at three different time instants obtained with Algorithm 3.1 and $\alpha = 1$.

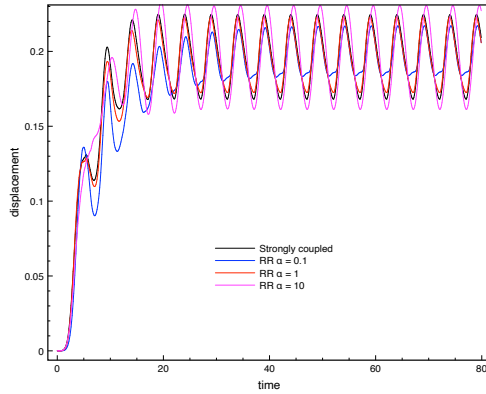


FIG. 6. Time history of the mid-point displacement magnitude obtained with Algorithm 3.1, for three different values of α , and a strongly coupled scheme.

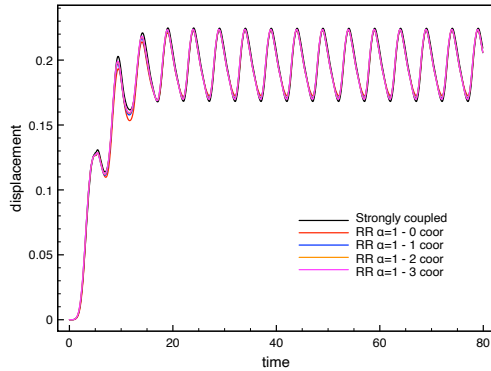


FIG. 7. Time history of the interface mid-point displacement magnitude obtained with Algorithm 3.1, for $\alpha = 1$ and different correction iterations, and a strongly coupled scheme.

414 The system is described by the non-linear coupled problem (2.1)-(2.3) in which
 415 the solid model (2.2) is replaced by a non-linear Timoshenko beam (see, e.g., [3]). The
 416 overall system is initially at rest and an oscillating shear velocity profile is imposed on
 417 the upper boundary $\mathbf{u}(t) = (1 - \cos(0.4\pi t), 0)^T$ on $[0, 1] \times \{1\}$. A no-slip condition is
 418 enforced on the portions $\{0, 1\} \times [0, 0.9]$ of the lateral cavity walls, and zero traction
 419 is prescribed on the remaining parts $\{0, 1\} \times [0.9, 1]$. The fluid physical parameters are

420 given by $\rho^f = 1.0$ and $\mu = 0.01$, and for the solid $\rho^s = 250$, $\epsilon = 0.002$, $E = 250$ and
 421 $\nu = 0$.

422 The spatial fluid approximation in (3.11) is made of $\mathbb{Q}_1/\mathbb{Q}_1$ finite elements with
 423 a SUPG/PSPG stabilized formulation. Linear MITC beam elements are used for the
 424 approximation of the Timoshenko beam in (3.10). In this numerical example, the
 425 computational meshes for the fluid and the solid meshes are, respectively, made of
 426 400 quadrilaterals and of 20 segments and a time-step length of $\tau = 0.1$ is considered.
 427 All the numerical computations have been performed with the FELiScE library¹.

428 For illustration purposes, we have reported in Figure 5 some snapshots of the fluid
 429 velocity magnitude in the current configuration at different time-instants, obtained
 430 with Algorithm 3.1 and $\alpha = 1$. We now focus on the accuracy of this loosely coupled
 431 scheme. To this purpose, we have first reported in Figure 6 the magnitude of the
 432 interfacial mid-point displacement obtained with Algorithm 3.1, for different values
 433 of α , and with a strongly coupled scheme. The impact of α on the accuracy is
 434 clearly visible. As in the previous numerical example (Section 5.1), the accuracy of
 435 Algorithm 3.1 degrades when α is both smaller and larger than the optimal value
 436 (here, around $\alpha = 1$). It is also worth noting the very good accuracy of the results
 437 obtained with Algorithm 3.1 and $\alpha = 1$. Indeed, without any correction iteration
 438 the proposed loosely coupled scheme delivers practically the same accuracy as the
 439 strongly coupled scheme. This observation is in line with the results of the previous
 440 section (Figures 1–3) and the error estimate of Theorem 2, which indicate that small
 441 values of the solid elastic parameters yield a low splitting error.

442 Finally, Figure 7 compares the results obtained with Algorithm 3.1 for $\alpha = 1$ and
 443 different correction iterations. We recall that one correction iteration corresponds to
 444 performing once more steps (3.10), (3.11) and (3.12) of Algorithm 3.1 with updated
 445 Robin conditions, that is, by initializing $\boldsymbol{\lambda}^{n-1}$ and $\hat{\mathbf{u}}^{n-1}|_{\Sigma}$ with the last values of $\boldsymbol{\lambda}^n$
 446 and $\hat{\mathbf{u}}^n|_{\Sigma}$. Since the accuracy is already very good without any correction, it only
 447 slight improves as we increase the number of corrections.

448 **5.3. Pressure wave in an elastic tube.** We consider the 3D non-linear coun-
 449 terpart of the numerical example considered in Section 5.1, viz., the propagation of a
 450 pressure wave within an elastic tube (see, e.g., [18, Chapter 12]). The fluid domain is
 451 a straight tube of radius 0.5 and length 5. The vessel wall has a thickness of 0.1. All
 452 the units are given in the CGS system. The fluid-structure system is modeled by the
 453 non-linear coupled problem (2.1)-(2.3). The overall system is initially at rest and an
 454 over pressure of $1.3332 \cdot 10^4$ is imposed on the inlet boundary during the time interval
 455 $[0, 0.005]$. The solid wall is clamped at its extremities. The physical parameters for
 456 the fluid are $\rho^f = 1$ and $\mu = 0.035$, and for the solid $\rho^s = 1.2$, $E = 3 \cdot 10^6$ and $\nu = 0.3$.
 457 In (3.10) and (3.11) continuous \mathbb{P}_1 finite elements are used (a SUPG/PSPG stabilized
 458 formulation is considered in the fluid). All the numerical computations have been
 459 performed with the FELiScE library.

460 To highlight the fluid-structure interaction in this numerical example, Figure 8
 461 shows snapshots of the fluid pressure in the deformed configuration at different time-
 462 instants, obtained using Algorithm 3.1 with $\alpha = 500$. We will now assess the influence
 463 of the parameter α . In Figure 9, we display the magnitude of the interfacial mid-point
 464 displacement calculated using Algorithm 3.1 for various α values. These results are
 465 then compared to those obtained using a strongly coupled scheme. As observed in the
 466 previous numerical examples, the performance of Algorithm 3.1 is closely linked to the

¹<https://gitlab.inria.fr/felisce/felisce>

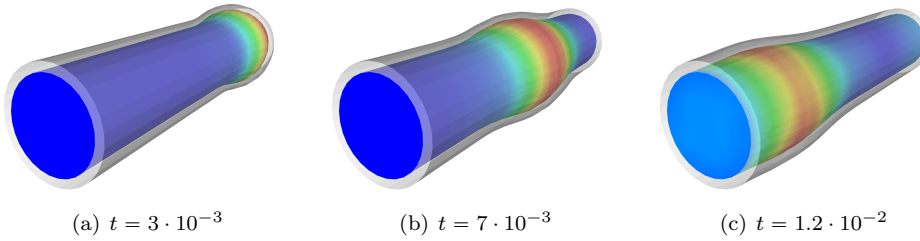


FIG. 8. *Snapshots of the fluid pressure in the deformed configuration at three different time instants with $\alpha = 500$.*

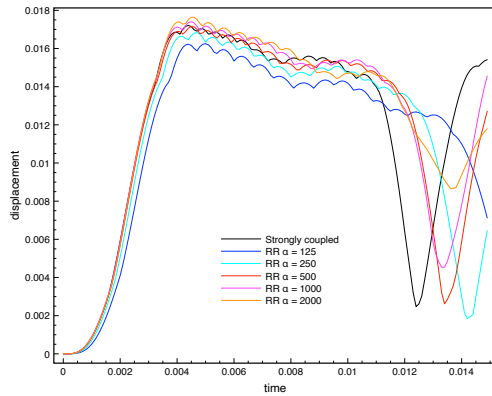


FIG. 9. *Time history of the interface mid-point displacement magnitudes with implicit coupling and RR algorithm with different α .*

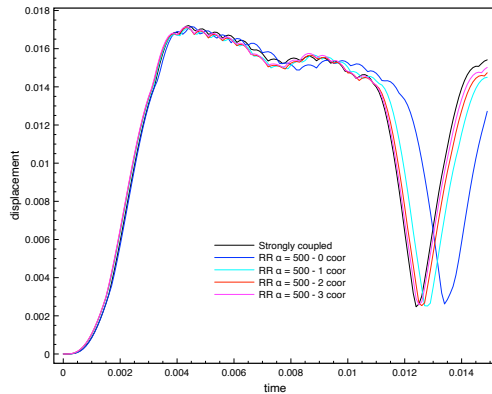


FIG. 10. *Time history of the interface mid-point displacement magnitudes with implicit coupling and RR algorithm with $\alpha = 500$ and different corrections.*

467 choice of α . Specifically, Algorithm 3.1 shows good accuracy when α is approximately
 468 500. However, as we deviate from this range, both smaller and larger values of α tend
 469 to degrade the accuracy.

470 Figure 10 illustrates the impact of some correction iterations in Algorithm 3.1
 471 with $\alpha = 500$. We observe an improvement in the accuracy of Algorithm 3.1 as

472 we increase the number of corrections. It is worth noting that a single iteration
 473 significantly improves the accuracy. Large values of the solid physical parameters can
 474 negatively impact the solution, necessitating correction iterations to achieve accurate
 475 results.

476 **6. Conclusion.** We have extended the stability results of the loosely coupled
 477 Robin-Robin coupling from [5] to the fully nonlinear case. A nearly-optimal error
 478 estimate was also reported for the linear case. The numerical section validated the
 479 theoretical results, but also pointed to the importance of making a judicious choice
 480 of the Robin parameter α in order to observe optimal convergence in the range of
 481 discretization parameters used.

482

REFERENCES

- 483 [1] S. BADIA, F. NOBILE, AND C. VERGARA, *Robin-Robin preconditioned Krylov methods for*
 484 *fluid-structure interaction problems*, *Comput. Methods Appl. Mech. Engrg.*, 198 (2009),
 485 pp. 2768–2784, <https://doi.org/10.1016/j.cma.2009.04.004>, <https://doi.org/10.1016/j.cma.2009.04.004>.
 486
 487 [2] J. W. BANKS, W. D. HENSHAW, AND D. W. SCHWENDEMAN, *An analysis of a new stable*
 488 *partitioned algorithm for FSI problems. Part I: Incompressible flow and elastic solids*, *J.*
 489 *Comput. Phys.*, 269 (2014), pp. 108–137, <https://doi.org/10.1016/j.jcp.2014.03.006>, <https://doi.org/10.1016/j.jcp.2014.03.006>.
 490
 491 [3] K. BATHE, *Finite Element Procedures*, Prentice Hall, 1996.
 492 [4] F. BREZZI AND J. PITKÄRANTA, *On the stabilization of finite element approximations of the*
 493 *Stokes equations*, in *Efficient solutions of elliptic systems* (Kiel, 1984), vol. 10 of *Notes*
 494 *Numer. Fluid Mech.*, Vieweg, 1984, pp. 11–19.
 495 [5] E. BURMAN, R. DURST, M. FERNÁNDEZ, AND J. GUZMÁN, *Fully discrete loosely coupled Robin-*
 496 *Robin scheme for incompressible fluid-structure interaction: stability and error analy-*
 497 *sis*, *Numer. Math.*, 151 (2022), pp. 807–840, <https://doi.org/10.1007/s00211-022-01295-y>,
 498 <https://doi.org/10.1007/s00211-022-01295-y>.
 499 [6] E. BURMAN, R. DURST, M. FERNÁNDEZ, AND J. GUZMÁN, *Loosely coupled, non-iterative time-*
 500 *splitting scheme based on Robin-Robin coupling: unified analysis for parabolic/parabolic*
 501 *and parabolic/hyperbolic problems*, *J. Numer. Math.*, 31 (2023), pp. 59–77, <https://doi.org/10.1515/jnma-2021-0119>, <https://doi.org/10.1515/jnma-2021-0119>.
 502 [7] E. BURMAN, R. DURST, AND J. GUZMÁN, *Stability and error analysis of a splitting method using*
 503 *Robin-Robin coupling applied to a fluid-structure interaction problem*, *Numer. Methods*
 504 *Partial Differential Equations*, 38 (2022), pp. 1396–1406, <https://doi.org/10.1002/num.22840>, <https://doi.org/10.1002/num.22840>.
 505 [8] E. BURMAN AND M. FERNÁNDEZ, *Stabilization of explicit coupling in fluid-structure interac-*
 506 *tion involving fluid incompressibility*, *Comput. Methods Appl. Mech. Engrg.*, 198 (2009),
 507 pp. 766–784, <https://doi.org/10.1016/j.cma.2008.10.012>, <https://doi.org/10.1016/j.cma.2008.10.012>.
 508 [9] E. BURMAN AND M. FERNÁNDEZ, *Explicit strategies for incompressible fluid-structure inter-*
 509 *action problems: Nitsche type mortaring versus Robin-Robin coupling*, *Internat. J. Numer.*
 510 *Methods Engrg.*, 97 (2014), pp. 739–758, <https://doi.org/10.1002/nme.4607>, <https://doi.org/10.1002/nme.4607>.
 511 [10] E. BURMAN, M. FERNÁNDEZ, AND P. HANSBO, *Continuous interior penalty finite element*
 512 *method for Oseen's equations*, *SIAM J. Numer. Anal.*, 44 (2006), pp. 1248–1274.
 513 [11] P. CAUSIN, J. F. GERBEAU, AND F. NOBILE, *Added-mass effect in the design of partitioned*
 514 *algorithms for fluid-structure problems*, *Comput. Methods Appl. Mech. Engrg.*, 194 (2005),
 515 pp. 4506–4527, <https://doi.org/10.1016/j.cma.2004.12.005>, <https://doi.org/10.1016/j.cma.2004.12.005>.
 516 [12] R. DURST, *Recent Advances in Splitting Methods Based on Robin-Robin Coupling Condi-*
 517 *tions*, PhD thesis, Brown University, 2022, [https://repository.library.brown.edu/studio/](https://repository.library.brown.edu/studio/item/bdr:v34deskr/)
 518 [item/bdr:v34deskr/](https://repository.library.brown.edu/studio/item/bdr:v34deskr/).
 519 [13] C. FARHAT, P. GEUZAINÉ, AND C. GRANDMONT, *The discrete geometric conservation law and*
 520 *the nonlinear stability of ale schemes for the solution of flow problems on moving grids*,
 521 *Journal of Computational Physics*, 174 (2001), pp. 669–694.
 522 [14] C. FARHAT, M. LESOINNE, AND P. LETALLEC, *Load and motion transfer algorithms for*

- 528 *fluid/structure interaction problems with non-matching discrete interfaces: momentum*
529 *and energy conservation, optimal discretization and application to aeroelasticity*, *Comput. Methods Appl. Mech. Engrg.*, 157 (1998), pp. 95–114, [https://doi.org/10.1016/](https://doi.org/10.1016/S0045-7825(97)00216-8)
530 [S0045-7825\(97\)00216-8](https://doi.org/10.1016/S0045-7825(97)00216-8), [https://doi.org/10.1016/](https://doi.org/10.1016/S0045-7825(97)00216-8)
531 [S0045-7825\(97\)00216-8](https://doi.org/10.1016/S0045-7825(97)00216-8).
- [15] M. FERNÁNDEZ, L. FORMAGGIA, J.-F. GERBEAU, AND A. QUARTERONI, *The derivation of*
532 *the equations for fluids and structures*, in *Cardiovascular mathematics*, vol. 1 of MS&A.
533 *Model. Simul. Appl.*, Springer Italia, Milan, 2009, pp. 77–121, [https://doi.org/10.1007/](https://doi.org/10.1007/978-88-470-1152-6_3)
534 [978-88-470-1152-6_3](https://doi.org/10.1007/978-88-470-1152-6_3), https://doi.org/10.1007/978-88-470-1152-6_3.
535
- [16] M. FERNÁNDEZ, J. MULLAERT, AND M. VIDRASCU, *Generalized Robin-Neumann explicit cou-*
536 *pling schemes for incompressible fluid-structure interaction: stability analysis and numer-*
537 *ics*, *Internat. J. Numer. Methods Engrg.*, 101 (2015), pp. 199–229.
538
- [17] M.-A. FERNÁNDEZ AND J.-F. GERBEAU, *Algorithms for fluid-structure interaction problems*,
539 in *Cardiovascular mathematics*, vol. 1 of MS&A. *Model. Simul. Appl.*, Springer, 2009,
540 pp. 307–346.
541
- [18] L. FORMAGGIA, A. QUARTERONI, AND A. VENEZIANI, eds., *Cardiovascular Mathematics. Mod-*
542 *eling and simulation of the circulatory system*, vol. 1 of *Modeling, Simulation and Appli-*
543 *cations*, Springer, 2009.
544
- [19] C. FÖRSTER, W. WALL, AND E. RAMM, *Artificial added mass instabilities in sequential staggered*
545 *coupling of nonlinear structures and incompressible viscous flows*, *Comput. Methods Appl.*
546 *Mech. Engrg.*, 196 (2007), pp. 1278–1293.
547
- [20] O. GONZALEZ, *Exact energy and momentum conserving algorithms for general models in non-*
548 *linear elasticity*, *Computer Methods in Applied Mechanics and Engineering*, 190 (2000),
549 pp. 1763–1783.
550
- [21] P. HANSBO, J. HERMANSSON, AND T. SVEDBERG, *Nitsche’s method combined with space-time*
551 *finite elements for ALE fluid-structure interaction problems*, *Comput. Methods Appl.*
552 *Mech. Engrg.*, 193 (2004), pp. 4195–4206, <https://doi.org/10.1016/j.cma.2003.09.029>,
553 <https://doi.org/10.1016/j.cma.2003.09.029>.
554
- [22] F. HECHT, *New development in FreeFem++*, *J. Numer. Math.*, 20 (2012), pp. 251–265.
555
- [23] L. SCOTT AND S. ZHANG, *Finite element interpolation of nonsmooth functions satisfying bound-*
556 *ary conditions*, *Mathematics of Computation*, 54 (1990), pp. 483–493.
557
- [24] A. SEBOLDT AND M. BUKAČ, *A non-iterative domain decomposition method for the interaction*
558 *between a fluid and a thick structure*, *Numer. Methods Partial Differential Equations*, 37
559 (2021), pp. 2803–2832.
560
- [25] S. SMALDONE, *Numerical analysis and simulations of coupled problems for the cardiovascular*
561 *system*, PhD thesis, Université Pierre et Marie Curie, 2014. [https://tel.archives-ouvertes.](https://tel.archives-ouvertes.fr/tel-01287506)
562 [fr/tel-01287506](https://tel.archives-ouvertes.fr/tel-01287506).
563
- [26] T. TEZDUYAR, *Stabilized finite element formulations for incompressible flow computations*,
564 vol. 28 of *Advances in Applied Mechanics*, Elsevier, 1991, pp. 1–44, [https://doi.org/](https://doi.org/https://doi.org/10.1016/S0065-2156(08)70153-4)
565 [https://doi.org/https://doi.org/10.1016/S0065-2156\(08\)70153-4](https://doi.org/https://doi.org/10.1016/S0065-2156(08)70153-4), [https://www.sciencedirect.com/science/](https://www.sciencedirect.com/science/article/pii/S0065215608701534)
566 [article/pii/S0065215608701534](https://www.sciencedirect.com/science/article/pii/S0065215608701534).
567